



Applied Physics Laboratory

University of Washington

1013 NE 40th Street
Box 355640
Seattle, WA 98105-6698

206-543-1300
FAX 206-543-6785
www.apl.washington.edu

30 January 2017

To: Dr. Raymond J. Soukup
Office of Naval Research (ONR 322)
875 N. Randolph Street, Suite 1425
Arlington, VA 22203-1995

From: Brian Todd Hefner

Subj: ONR Grant: N00014-13-1-0040
“Broadband Scattering from Sand and Sand/Mud Sediments with Extensive Environmental Characterization”

Encl: (1) Final Report including publications for “Broadband Scattering from Sand and Sand/Mud Sediments with Extensive Environmental Characterization” with accompanying SF 298.
(2) Submitted publication (draft) to IEEE Journal of Oceanic Engineering: “Characterization of Seafloor Roughness to Support Modeling of Mid-Frequency Reverberation”
(3) Submitted publication (draft) to IEEE Journal of Oceanic Engineering: “High-frequency sound speed and attenuation measurements in sandy sediments with a portable velocimeter.”
(4) Proceedings from the 2nd International Conference and Exhibition on Underwater Acoustics: “Overview of the Reverberation Component of TREX13.”
(5) Proceedings from the Institute of Acoustics: “High-Frequency Scattering from a Muddy Sand Sediment with an Overlying Mud Layer.”

Enclosed please find the Final Report with publications and corresponding SF 298 form (1) for the subject grant. Enclosures (2) through (5) are other articles and presentations. These documents constitute the Final Technical Report and deliverables for ONR Grant N00014-13-1-0040.

cc: ONR Seattle – Evan Wood and Kyoohui Beal
Naval Research Laboratory Code 5596 via FedEx
Defense Technical Information Center
Office of Sponsored Programs – UW Closeout
APL-UW Grants and Contracts Closeout Coordinator

Final Report

Broadband Scattering from Sand and Sand/Mud Sediments with Extensive Environmental Characterization

Brian Todd Hefner

Applied Physics Laboratory, University of Washington, 1013 NE 40th Street, Seattle, WA 98105
phone: (206) 616-7558 fax: (206) 543-6785 email: hefner@apl.washington.edu

Award Number: N00014-13-1-0040

<http://oa.apl.washington.edu>

RESEARCH GOALS

The goal of this research was to study mid-to-high frequency scattering from the seafloor to determine the dominant scattering mechanisms, potentially addressing questions left unresolved from the previous sediment acoustics experiments, SAX99 and SAX04. This work was also to provide environmental characterization to support the analysis of data collected during the Target and Reverberation Experiment in 2013 (TREX13) as well as the St. Andrew's Bay experiment in 2014 (BayEx14).

TECHNICAL APPROACH

FY13

The mid-frequency transducers will be mounted to the tower prior to deployment during TREX13. The data will be collected on both tower-mounted systems during the experiment and the BSS will be deployed from a dive boat along the TREX13 reverberation track. Environmental characterization will be performed with a number of systems, deployed by both APL-UW and other institutions. This environmental data will be compiled as part of this project to both support model comparisons for the backscatter strength measurements as well as for the main TREX13 measurements.

Accomplishments:

TREX13 took place as planned from April 5 – June 7, 2013 with Dr. DJ Tang and myself acting as Co-Chief Scientists for the reverberation component of the experiment and Drs. Kevin Williams and Steve Kargl acting as Co-Chief Scientists for the target scattering component. The APL-UW rail system was deployed from May 25 – June 8, 2013 during which time scattering data was collected from 30 – 500 kHz at grazing angles from 15 to 40 degrees. Due to technical difficulties prior to the start of the experiment, the number of measurements conducted were significantly reduced and were collected towards the end of the rail system deployment when the presence of fish had become a major issue in the experiment. Detailed analysis of the data was

delayed due to the need to recalibrate the transducers in the Fall of 2013. Analysis of the high-frequency data confirmed the results of the data collection during the pilot experiment in 2012: roughness scattering dominates below the critical angle at this site, while scattering from shells in the sediment volume dominate above critical angle. The lower frequency data has proven more problematic to analyze due to the presence of both the fish and interference from the structural elements of the rail system.

Following the recovery of the rail system, the APL-UW seafloor laser-line scanner (SLS) was deployed at multiple locations at the TREX13 site to measure seafloor roughness. The sediment showed significant spatial variability and while we were only able to collect a limited number of roughness measurements in the time available, correlations of the roughness parameters with the backscatter survey data collected by Drs. Chris DeMoustier and Barbara Kraft using a multibeam echosounder made it possible to develop a model for the seafloor roughness throughout the experiment site.

Immediately after the SLS deployment, sediment sampling and high-frequency sound speed and attenuation measurements were made at a number of locations around the TREX13 site. The sound speed and attenuation measurements were conducted in collaboration with Dr. Laurent Guillon from the Research Institute of the French Naval Academy and Xavier Demoulin from Maree, a French company specializing in underwater acoustics. Their participation in TREX13 was supported by the Visiting Scientists Program at ONR Global. Measurements were made using the INvestigation of SEdiments by Acoustics (INSEA) instrument which is a diver deployed and operated acoustic array to make time-of-flight sound speed and attenuation measurements in the seafloor. This was accompanied by the collection of diver cores and shell samples from small cofferdams at the same locations. As was the case for scattering from the seafloor, the data collected by the INSEA indicate that shells play an important role in propagation within the seafloor at the TREX13 site.

FY14

As part of BayEx14, the tower will again be deployed and the tower-mounted sonars will collect backscatter data at the experiment site. The BSS will also be deployed from a boat of opportunity during this experiment as well. The environmental characterization of the BayEx14 target field will be coordinated under this proposal and used to support both the backscatter measurements and the main BayEx14 experiments.

Accomplishments:

In May 2014, the APL rail tower was deployed in St. Andrews Bay, FL off the shore of Shell Island. The sediment consisted of the 15 cm mud layer overlying a muddy, coarse sand basement. Scattering data was again collected as well as high-frequency multibeam data. Environmental characterization at the site included roughness measurements using the SLS, sediment heterogeneity measurements using the IMP2 conductivity probe, analysis of diver cores for porosity and density within both the mud layer and in the sand basement, and sound speed and attenuation measurements. The environmental data was analyzed and provided to the experiment teams from APL-UW, NSWC PCD, and MIT.

While the Bottom Backscatter Sonar (BBS, formerly BSS) was deployed during TREX13, questions about the data led us to redeploy the instrument at the TREX13 site in 2014. Backscatter data was collected from both the sand ridges and mud-filled swales and subsequent analysis of the data found that while roughness was the dominant scattering mechanism at 3 kHz below the critical angle on the sand ridges, volume scattering was dominant for the swales. Using data from both the BBS and NSWC PCD Bottom/Buried Object Scanning Sonar (BOSS), it was found that the volume scattering is due to a layer of heterogeneities 25 cm beneath the sediment interface in both cases. Above the critical angle, volume scattering is the dominant scattering mechanism for both the sand ridges and the swales. While we had planned to deploy the BBS at the BayEx14 site, the shallow water depth and difficulties working in the bay after the main experiment, made this impractical.

FY15-FY16

Analysis and data/model comparisons will continue into the final year of this proposal leading to eventual distribution and incorporation into the final reverberation and target scattering data sets.

Accomplishments:

Efforts during these two years focused on analysis of the data collected during both experiments. In addition to this work, data collected in the NSWC PCD test pond in 2010 has also been revisited. This was motivated by a reassessment of the IMP2 conductivity probe and historic data collected with this system. While the IMP2 was not in operation during the 2010 experiment, data from 2006 was found which could provide the missing environmental characterization for model/data comparisons. This complete characterization of the pond sediment made it possible to fully test the scattering models as well models of scattering loss within the sediment.

The analysis of data from TREX13 and efforts to continue collaboration with the participants from that experiment led to several workshops to discuss and share results from the experiment. The workshops were organized by Dr. Tang and myself and took place after the 2013 Fall ASA meeting in San Francisco, CA, the 2014 Fall ASA meeting in Indianapolis, IN, and finally culminating in a workshop which followed the 2016 IEEE Oceans meeting in Monterey, CA. At this last workshop, the final analysis results were presented from a number of the participants and a comprehensive environmental characterization of the TREX13 site, incorporating many of the participants' results, was put forward.

Many of the results presented at that workshop will be included in the upcoming TREX13 special collection in the IEEE Journal of Oceanic Engineering, for which Dr. Tang and I are the guest editors. Significant efforts have been devoted in FY15 and FY16 to preparation of manuscripts for this collection.

Publications:

1. Hefner, B.T., and D. Tang (2014), "Overview of the reverberation component of TREX13", Proc., 2nd International Conference and Exhibition on Underwater Acoustics, 22-27 June, Rhodes, Greece, 144, 2014.

2. Hefner, B. T., A. Ivakin, and D. Jackson (2015), "High-frequency scattering from a muddy sand sediment with an overlying mud layer," In: Proc. Institute of Acoustics. Vol. 37 (1), pp. 63– 70.
3. Penko, A., J. Calantoni, and B.T. Hefner (2017), "Modeling and observations of sand ripple formation and evolution during TREX13," Accepted to the IEEE J. of Oceanic Eng., TREX13 special collection.
4. Hefner, B.T. (2017), "Characterization of seafloor roughness to support modeling of mid-frequency reverberation," Submitted to the IEEE J. of Oceanic Eng., TREX13 special collection.
5. Demoulin, X., L. Guillon, and B.T. Hefner (2017), "High-frequency sound speed and attenuation measurements in sandy sediments with a portable velocimeter," Submitted to the IEEE J. of Oceanic Eng., TREX13 special collection.
6. Tang, D., B.T. Hefner, and D.R. Jackson (2017), "Direct-path backscatter measurements along the main reverberation track of TREX13," Submitted to the IEEE J. of Oceanic Eng., TREX13 special collection.
7. Yang, J., D. Tang, B.T. Hefner, K.L. Williams, and J.R. Preston (2017), "Overview of mid-frequency reverberation data acquired during the Target and Reverberation Experiment 2013," Submitted to the IEEE J. of Oceanic Eng., TREX13 special collection.
8. Hefner, B.T. (2017), "High-frequency acoustic backscattering from a well-characterized sand sediment," In preparation for the J. Acoust. Soc. Am.
9. Hefner, B.T., A. Ivakin, and D.R. Jackson (2017), "High-frequency scattering from shells within a sand sediment," In preparation for the IEEE J. Oceanic Eng.

Characterization of Seafloor Roughness to Support Modeling of Mid-Frequency Reverberation

Brian T. Hefner

Abstract

A seafloor laser scanner (SLS) was deployed in the Gulf of Mexico during the 2013 Target and Reverberation Experiment (TREX13). This system collected digital elevation maps at 14 locations along the main reverberation track, and these measurements provided roughness power spectra for modeling seafloor acoustic scattering. The spectra were divided into two regimes according to the mid- and high-frequency acoustic measurements made during the experiment. For the wavenumbers corresponding to the mid-frequency regime (2–4 kHz), the spectra could be approximated using the mean spectral exponent derived from the all of the spectra. With this spectral exponent, the best fit spectral strengths were found to be negatively correlated to the backscatter levels measured at 400 kHz using a multibeam echosounder (MBES). While the scattering mechanisms at 400 kHz are not influenced by the roughness at these low wavenumbers, this correlation may be indirectly related to the bioturbation and the spatial variation of the shell content. A more pronounced correlation was found for the high wavenumbers where again a single spectral exponent could be used to a good approximation. In this case, the spectral strengths were also linearly related to the MBES backscattering level but with a positive correlation. For these wavenumbers, the roughness is largely influenced by the shell content which is also the dominant scattering mechanism at 400 kHz. The correlations between the roughness and the MBES measurements provide a means to approximate the seafloor roughness parameters in both wavenumber regimes throughout the experiment site. For the low-wavenumber spectrum, an alternative approach is also proposed which uses the spectral parameters for the mean spectrum to approximate the roughness throughout the TREX13 site.

B. Hefner is with the Applied Physics Laboratory, University of Washington, Seattle, WA 98105 USA (e-mail: hefner@apl.washington.edu).

Index Terms

TREX13, acoustic scattering, scattering parameters measurement, sediments, seafloor roughness.

I. INTRODUCTION

While a number of environmental variables affect reverberation in shallow water, scattering from the seafloor typically dominates the backscatter. These bottom scattering contributions are generally attributed to either rough surface scattering at the sediment interface or scattering from continuous or discrete heterogeneities in the sediment volume[1]. While the surface scattering and volume scattering cross-sections can be characterized separately, they are often conflated into a single scattering cross-section that is determined from an empirical fit to the acoustic data. While this conflated cross-section may provide limited knowledge about the acoustics of a particular site, generalizations of these fits to other environments can result in highly inaccurate model predictions. In applying acoustic propagation and reverberation models, users therefore seek to determine the minimum amount of environmental knowledge needed to obtain an acceptable amount of accuracy in the model prediction. One of the goals of the Target and Reverberation Experiment conducted in the Spring of 2013 (TREX13) is to evaluate these different environmental factors and determine their significance for different applications. To accomplish this, extensive environmental characterization was performed during TREX13.

To evaluate the contribution of rough surface scattering from the seafloor, a seafloor laser scanner (SLS) was deployed at various locations along the main reverberation track during TREX13. This system uses structured lighting to measure seafloor roughness at the length scales relevant to the acoustic measurements made during the experiment. These acoustic measurements were conducted at both 2–10 kHz and 100–400 kHz. To support this broad range of frequencies, the SLS measured the micro-topography with a horizontal resolution of 1 mm over a 30 cm \times 360 cm area. These digital elevation maps (DEM) can be used to determine the roughness power spectrum, a statistical input needed for various seabed scattering models.

The primary goal of TREX13 was to measure reverberation in shallow water with supporting environmental characterization. This characterization was to be extensive enough to determine the relative importance of each environmental parameter for accurate modeling of the measured reverberation. Reverberation measurements performed on the continental shelf are typically

conducted in water depths of 50–100 m and reverberation can be due to scattering from portions of the seafloor at ranges out to 10s of kilometers. Environmental characterization of the seafloor at these depths and over these ranges can be both difficult and costly. In order to overcome these difficulties, the TREX13 measurements were collected along a 19–20 m isobath, 2 km from Shell Island near Panama City Beach, Florida. This shallow depth ensured that the propagating sound had many interactions with the sea surface and seafloor while the reverberation contributions were limited to a maximum range of 5–7 km. The cross-range was also minimized by receiving on a horizontal line array (HLA) mounted on the seafloor[2]. The combination of shallow depth and HLA limited the region for environmental characterization to approximately 5 km × 1 km.

The site was also chosen with the expectation that the seafloor was a sand sediment and the seafloor properties would be constant along the track. A multibeam echosounder (MBES) survey conducted by C. DeMoustier and B. Kraft prior to the start of the experiment found that the 400 kHz MBES backscatter from the seafloor varied significantly over the site[3]. Subsequent sediment sampling found that these variations were due to changes in the sediment shell content and the presence of narrow mud-filled areas running perpendicular to the main reverberation track. Due to time constraints, it was not possible measure the seafloor roughness with sufficient coverage along the track to capture this variability. While the roughness was measured at only 14 locations, these measurements cover the range of sediment variability at the site and by correlating these measurements with the 400 kHz backscatter survey it is possible to infer the roughness parameters throughout the experiment site.

A secondary goal of the measurements reported here was to examine the spatial distribution of roughness affecting high-frequency scattering from the sediment. A number of experiments have been conducted in the Gulf of Mexico off the coast of the Florida panhandle to examine high-frequency scattering from the seafloor with a particular emphasis on its role in mine countermeasures. These include the Coastal Benthic Boundary Layer (CBBL) program[4], [5] and the 1999 and 2004 Sediment Acoustics Experiments (SAX99 and SAX04)[6], [7], [8]. While extensive roughness measurements were made as part of these experiments, questions remained about the spatial distribution of the roughness and whether the roughness could be treated as statistically stationary[9]. During these previous experiments, roughness measurements were typically made in the vicinity of the acoustic measurements, usually confined to areas with a radius on the order of 50 m. The experiment site at TREX13 provides the opportunity cover

a much larger area and to examine how the roughness varies within the site.

After first describing the SLS and the processing necessary to extract the roughness power spectra from the measured DEMs in Section II, the spectral parameters for each measurement location are discussed in Section III. These spectral parameters are then compared to the co-located backscattering levels to extract relationships that can be used to map the spectral parameters throughout the survey area. The mechanisms that may be driving these relationships and the implications of the spatial distribution of the roughness are discussed in Section IV.

II. METHODS

The Seafloor Laser-line Scanner (SLS) is a structural-light-based system developed and tested in collaboration with CC Wang at the Institute of Applied Marine Physics and Undersea Technology, National Sun Yat-sen University[10], [11]. It consists of a laser line projector, a charge-coupled device (CCD) camera, and a PC control unit. The laser and camera are mounted on a rigid frame that maintains the relative position and orientation between the camera and the laser line source. The camera is a Basler A102f CCD with an image size of 1388×1038 pixels. The water depth at the TREX13 site was approximately 19 m and as a result there was a significant amount of ambient light at the seafloor during daytime operations. A green laser would typically be used for underwater applications, but the ambient light had a tendency to wash out a green laser line. To overcome this difficulty a red laser was used (635 nm) and a 400–700 nm lens filter was attached to the camera to remove a majority of the ambient light from the image. A cylindrical lens was placed in front of the beam to generate a 60° fan angle.

The camera, projector, and housing were mounted on the In-situ Measurement of Porosity 2 (IMP2) system. The IMP2 was designed to measure conductivity within the sediment from which the local porosity can be determined[12]. The system uses a probe that is attached to a horizontal and vertical linear stage which can insert the probe into the sediment along a 4 m track. The SLS assembly was mounted on the horizontal linear stage, 75 cm above the seafloor to achieve an effective scanning swath width of 30 cm. The CCD camera was tilted downward to face the laser projection on the seafloor at a 30° grazing angle. With this configuration, the optical resolution on the scanning plane (across track) is 0.3 mm. In each image frame, the high-contrast pixels correspond to the reflection of the laser line from the seafloor. With a calibrated camera, the pixels on the laser line can be converted into the height of the bottom profile at the

scan location[13].

As the IMP2 linear stage moves, the laser is scanned along the track. The resolution along the track depends on the speed of the linear stage and the frame rate of the CCD. The IMP2 linear stage speed was a constant 2.3 mm/s and the CCD frame rate was about 5-6 frames/s. This resulted in a scanning interval of approximately 0.5 mm. The actual location of each image frame along the track is inferred by comparing its acquisition time to that of the starting frame. This results in a digital elevation map (DEM) with dimensions of 30 cm \times 360 cm with 0.3- and 0.5-mm resolutions across and along the track, respectively, and 0.3 mm in the vertical direction. In practice, however, a 1.0 mm horizontal resolution was used in the DEM processing.

In addition to measuring the microtopography of the seafloor, the system also records the intensity of the laser light reflected at each point on the surface to produce a corresponding digital intensity map (DIM). This information, along with the microtopography in the DEM, makes it possible to identify objects on the bottom such as shells or biological organisms. Figure 1 gives an example of a subsection of the seafloor measured at site S4 by the SLS.

Each of the DEM is used to determine the 1D mean roughness power spectrum. The spectrum in the cross-track and along-track directions of the DEM is calculated; however, due to the narrow width of the DEM, the cross-track spectra are only applicable to the high-frequency acoustic data. For the DEM examined here, the cross-track spectra were consistent with the along-track spectra indicating that at the high wavenumbers, the roughness was isotropic. While the width of the DEM provided approximately 300 1-D spectra measured in the along-track direction at each site, there were an order of magnitude more spectra measured in the across-track direction. This resulted in a significant reduction in the statistical fluctuations in the across-track direction when the spectra were averaged. As a result, the 1-D spectra for each site are taken as a combination of the along-track spectra, which is used for wavenumbers less than 200 rad/m, and the across-track spectra, which is used for wavenumbers greater than 200 rad/m.

To determine the mean roughness power spectrum, the DEM are first windowed to remove any artifacts produced by blockages of the camera or laser. For example, in several deployments, cables attached to the system blocked the laser at one end of the track and the roughness could not be measured. This reduces the length or width of the DEM, but in all cases the lengths of the usable sections were still sufficient to give information about the low-wavenumber spectral strengths. A second pre-processing step is then performed to remove any spurious jumps in the

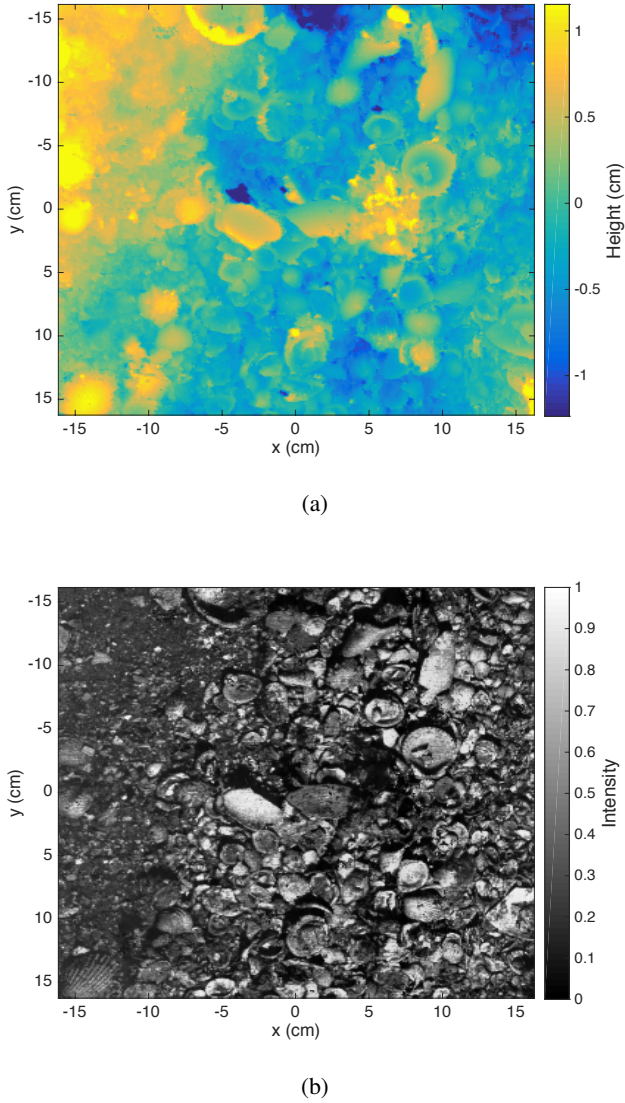


Fig. 1. Example of (a) a digital elevation map (DEM) and (b) a digital intensity map (DIM) collected at location S4.

surface height which could bias the roughness spectra. These spurious jumps can occur when the laser illuminates something in the water column or can't be seen by the camera because it is behind an object on the seafloor. For the TREX13 data, these jumps are associated with points on the seafloor where the laser line is behind the edge of a shell and can't be seen in the camera image. The removal of these jumps is accomplished by taking the gradient of the DEM and if the height changed abruptly by more than 1.0 cm, replacing that height by the mean value of the surrounding heights. This pre-processing step modified less than 0.1% of the points in each

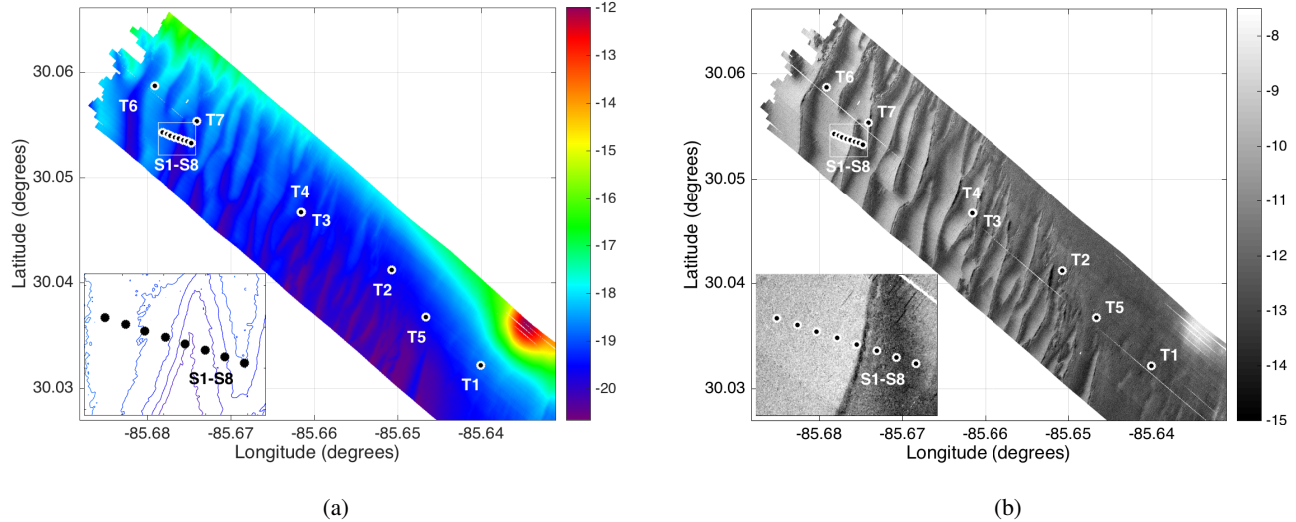


Fig. 2. SLS Deployment locations along the TREX13 main reverberation track in relation to the (a) bathymetry and (b) the backscatter level measured by DeMoustier and Kraft during the multibeam echosounder survey. The units of the color scale in (a) are meters relative to the mean sea level. The units of the gray scale in (b) are dB. The inset in each plot shows a close up view of location of sites S1-S8. For clarity, the bathymetry in the inset is shown as a contour plot where each contour represents a 28 cm change in bathymetry.

of the DEMs with the exception of Site S4 where 0.9% of the points were smoothed.

After pre-processing the following steps are performed to determine the 1-D roughness power spectrum along each line of surface heights in the along- and across-track directions:

- 1) The mean height is subtracted and any linear trend in the data is removed.
- 2) A Hann window is applied to the data to reduce spectral leakage.
- 3) Finally, the spectrum is determined from the fast Fourier transform of the data.

The mean roughness power spectrum is then found from the 1-D spectra.

The SLS was deployed from the R/V Hugh R. Sharp at 14 locations along the main reverberation track during TREX13. These locations are listed in Table I and plotted in Figure 2 relative to the backscatter and bathymetry measured by the multibeam sonar. Two sets of locations were chosen. The first set, labelled as T1–T7, corresponded to the locations where other TREX13 assets were deployed, such as the Scripps Vertical Line Arrays (VLAs). The second set, labelled as S1–S8 were chosen to densely sample a path that passed through one of the mud transitions identified in the multibeam backscatter. The primary goal of the second set of measurements was

TABLE I
LOCATIONS OF THE IMP2 SLS MEASUREMENTS AT THE TREX13 SITE SHOWN IN FIGURE 2.

Site	Longitude	Latitude
T1	30°1.902' N	85°38.400' W
T2	30°2.451' N	85°39.030' W
T3	30°2.788' N	85°39.676' W
T4	30°2.788' N	85°39.679' W
T5	30°2.719' N	85°38.789' W
T6	30°3.515' N	85°40.719' W
T7	30°3.313' N	85°40.422' W
S1	30°3.249' N	85°40.668' W
S2	30°3.240' N	85°40.637' W
S3	30°3.231' N	85°40.609' W
S4	30°3.222' N	85°40.578' W
S6	30°3.205' N	85°40.519' W
S7	30°3.196' N	85°40.490' W
S8	30°3.187' N	85°40.461' W

to support a separate effort on environmental characterization using multibeam sonars funded by the Strategic Environmental Research and Development Program (SERDP)[14]. Since this dataset was collected within the TREX13 main reverberation track and densely samples one of the transition regions, it is included in the current analysis. All of these measurements were collected from May 22 to May 26, 2013, after the reverberation measurements were completed.

At each measurement site, the SLS was lowered by crane to the bottom and remained cabled to the ship which held station using dynamic positioning. This made it possible to manually optimize the exposure settings of the camera and hence operate throughout the day and at different ambient light levels. No effort was made to control the orientation of the SLS and there were no means available to monitor the orientation once it was on the seafloor. For the high wavenumber portion of the spectrum this was not a problem since the seafloor was isotropic

in this region. For the low wavenumbers, several of the sites showed the presence of 30- to 50-cm wavelength sand ripples. While it was not possible to determine the orientation of these ripples from the DEM, diver observations and video indicate that the crests of these ripples ran parallel to shore and hence parallel to the main reverberation track. This is consistent with ripple generation by on-shore waves as would be expected given the water-depths and proximity to shore of the deployment sites. While this may not have an appreciable effect on the 2–4 kHz reverberation, the wavenumbers associated with these ripples are at or just below the low-wavenumber region of the spectrum discussed in the next section.

Two approaches will be taken to model the spectra measured at TREX13. The first involves fitting each spectrum with a model spectrum to find a unique set of spectral parameters for each site. This approach provides a good approximation to the roughness power spectra for each IMP2 deployment site and, assuming isotropy, the 2-D spectral parameters for that site can be determined. These spectral parameters can then be used to estimate roughness scattering strength using models such as first-order perturbation theory. While not addressed directly here, some care should be exercised when applying these models to the TREX13 site. Several of the SLS deployment locations had very high shell content both on and within the sediment which may have a stronger impact on seafloor scattering than the sediment roughness. Also, no effort is made here to separate the roughness associated with the sand/water interface from the roughness associated with the presence of shells.

The second approach attempts to identify correlations between the survey data collected at the site and the spectral parameters. These correlations are then used to make predictions about the spatial dependence of the roughness spectra. The TREX13 seafloor properties show significant spatial variability and the local roughness measurements reported in the next section were not collected at sufficient density to infer the spatial dependence of the spectral parameters. To overcome this, a remote sensing approach is taken here which leverages the high spatial coverage of the multibeam sonar survey by seeking correlations between the measured scattering levels and the spectral parameters. The survey was conducted by Drs. Chris DeMoustier and Barbara Kraft using a Teledyne-RESON SeaBat 7125 mounted in the well of the R/V Sharp. The survey of the main reverberation track was 7 km long and extended out to 0.75 km on either side of the track. The survey, conducted using the SeaBat operating at 400 kHz, generated a map of the bathymetry with a 50-cm horizontal resolution as well as a map of uncalibrated seafloor

backscatter levels. For these backscatter levels, the grazing angle dependence across the swath of the multibeam has been normalized by the mean backscatter level at each grazing angle across the entire survey area. Details of this data product are given in [3] and a portion of the backscatter map is shown in Figure 2b.

In order to determine if there was any correlation between the SLS spectral parameters and the MBES backscatter level, the backscatter data were averaged over $4\text{ m} \times 4\text{ m}$ patches centered on each SLS deployment site. The spectral parameters determined from the best fits to the spectrum measured at each site were then plotted as a function of the mean backscatter level to determine if there was any correlation between the parameters. Using this information, a set of spatially dependent spectral parameters are developed that can approximate the measured spectra and predict the spectral levels elsewhere at the site. Details of the approximation and the model choices motivating the approximation are given in Section III-B.

The remote sensing approach taken here differs from the typical echosounder survey inversions in that the focus at TREX13 is on a single bottom type, sand, which has varying amounts of shell. While the shell changes both the seafloor roughness and the volume heterogeneity within the sediment, the other geoacoustic properties remain approximately constant throughout the experiment site. Most other echosounder inversion approaches must contend with multiple bottom types for which changes in the backscatter response are the consequence of changes in several geoacoustic parameters. It may be possible to extend the approach taken here to other sediments and locations, but the application of this technique would require some care. Not only does this approach presuppose that the roughness parameters are related to the backscatter response, but the backscatter response would first need to be categorized according to sediment type. Correlations could then be sought between backscatter and ground truth data located within each of the sediment areas.

III. RESULTS

To provide an overview of the spectra measured across the TREX13 main reverberation track, each of the mean 1-D spectra measured along the IMP2 at each site is shown in Figure 3. As indicated in the figure and in the analysis that follows, the spectra have been divided into three regions: the low-wavenumber region (14.41 to 33.63 rad/m), the mid-wavenumber region (33.63 to 200 rad/m), and the high-wavenumber region (200 to 2500 rad/m). For the 7 km range over

TABLE II

THE POWER-LAW PARAMETERS DETERMINED FROM BEST FITS TO THE ALONG TRACK SPECTRUM MEASURED AT EACH POSITION. THE “LOW-WAVENUMBER” PARAMETERS WERE DETERMINED FROM A BEST LINEAR FIT IN THE LOG-LOG SCALE TO THE PORTION OF THE SPECTRA THAT IS RELEVANT TO MID-FREQUENCY ACOUSTIC SCATTERING BELOW THE CRITICAL ANGLE FOR THE TREX13 SITE. THE “HIGH-WAVENUMBER” PARAMETERS WERE DETERMINED FROM A BEST LINEAR FIT IN THE LOG-LOG SCALE TO THE PORTION OF THE SPECTRA RELEVANT TO HIGH-FREQUENCY ACOUSTIC SCATTERING.

Site	Low-wavenumber				High-wavenumber				L (cm)	
	Power-Law Parameters (14.4–33.6 rad/m)				Power-Law Parameters (200–2500 rad/m)					
	γ_{1L}	w_{1L} ($\times 10^3$ m $^{3-\gamma_{1L}}$)	$\sigma_{\gamma_{1L}}$	$\sigma_{w_{1L}}$ (dB m $^{3-\gamma_{1L}}$)	γ_{1H}	w_{1H} ($\times 10^3$ m $^{3-\gamma_{1H}}$)	$\sigma_{\gamma_{1H}}$	$\sigma_{w_{1H}}$ (dB m $^{3-\gamma_{1H}}$)		
T1	3.27	2.8723	0.85	11.57	2.01	0.0108	0.007	0.23	0.611	
T2	1.14	0.0015	0.50	6.83	1.96	0.0143	0.009	0.26	–	
T3	3.55	4.6127	0.75	10.38	1.96	0.0355	0.015	0.46	0.723	
T4	2.89	0.6857	0.56	7.58	1.97	0.0350	0.013	0.41	2.67	
T5	2.72	0.7752	1.38	18.85	1.79	0.0029	0.021	0.66	0.21	
T6	4.24	51.311	0.53	7.22	1.92	0.0108	0.018	0.54	0.64	
T7	3.47	3.9933	0.96	13.06	1.90	0.0406	0.019	0.59	1.52	
S1	4.53	206.5789	1.101	15.10	2.01	0.0505	0.012	0.36	1.21	
S2	3.64	7.4706	1.019	14.03	2.01	0.0464	0.009	0.29	1.56	
S3	3.73	7.8250	0.666	9.20	2.02	0.0559	0.014	0.43	0.94	
S4	1.04	0.0012	0.581	8.04	2.01	0.2103	0.014	0.44	–	
S6	2.87	1.2078	0.690	9.47	1.87	0.0048	0.009	0.28	0.37	
S7	3.13	2.4995	0.387	5.26	1.97	0.0076	0.013	0.40	0.25	
S8	3.53	12.6850	0.694	9.62	2.02	0.0158	0.011	0.34	0.86	

which the reverberation was measured during TREX13, the propagating modes correspond to grazing angles below the critical angle and first-order perturbation theory can be used to model the scattering [1]. The low-wavenumber region was thus chosen to correspond to the Bragg

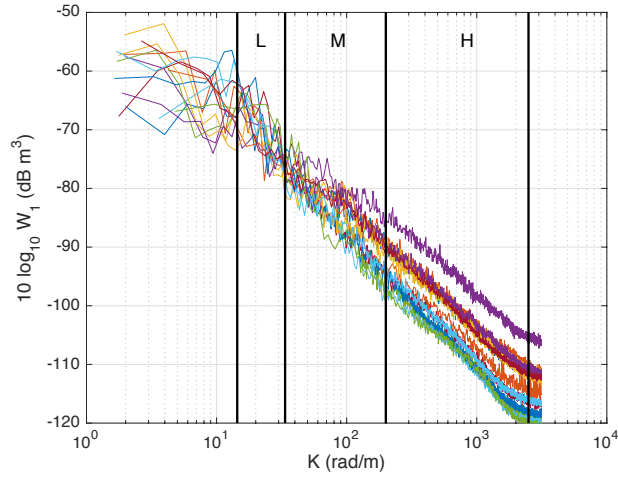


Fig. 3. All 1-D spectra measured along the long-axis of the IMP2 at the TREX13 site. The vertical lines denote the three wavenumber regions used to generate the power-law fits to the spectra: (L) the low-wavenumber region that is most relevant for the 2–4 kHz reverberation measurements, (H) the high-wavenumber region that is relevant to the high frequency multibeam backscatter measurements, and (M) the mid-wavenumber region.

wavenumbers needed to model subcritical, 2–4 kHz backscatter from the seafloor using first-order perturbation theory. The high-wavenumber region is based on observations and knowledge of the measured spectra. Starting at 200 rad/m, in both the along-track and the cross-track spectra, all of the spectra appear to follow a power-law until the very highest wavenumbers where noise becomes an issue. The upper wavenumber limit for this region (2500 rad/m) was chosen to correspond to the onset of noise in the cross-track spectra. The remaining portion of the spectra, the mid-wavenumber region, bridges the gap between the high- and low- wavenumber regions.

While the focus of the IMP2 deployments during TREX13 was to collect roughness data using the laser line scanner, at Site T6 the IMP2 was also used to make measurements using the conductivity probe. As described in the previous section, the probe was primarily designed to measure local porosity, but the abrupt change in conductivity at the sediment interface makes it possible to measure a 1-D roughness profile as well[12]. A comparison of the roughness power spectrum measured using these two methods at Site T6 is shown in Fig. 4. This comparison provides a valuable confirmation that the SLS was working properly during the deployment in that the spectra compare quite well, especially in the low-wavenumber region. In this comparison,

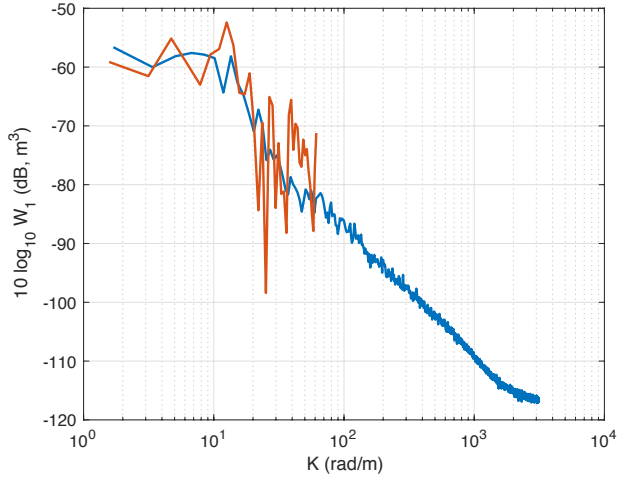


Fig. 4. Comparison of the roughness power spectra measured at Site T6 using the SLS (blue line) and the IMP2 conductivity probe. The SLS spectrum is the 1-D marginal spectrum determined from the average of 1-D spectra along the long-axis of the IMP2. The conductivity probe spectrum is determined from a single roughness profile.

the SLS spectrum is an average of many 1-D spectra while the conductivity probe spectrum is determined from a single roughness profile. As a consequence, the conductivity probe spectrum is much noisier and this likely accounts for the discrepancy in the spectra around $k = 45$ rad/m.

A. Individual Power-Law Spectral Fits

As discussed above, the low-wavenumber region contains those wavenumbers most relevant to 2–4 kHz, low-grazing angle backscatter. Within this region a majority of the spectra can be well-approximated as a power-law,

$$W_{1L}(k) = \frac{w_{1L}}{k^{\gamma_{1L}}}, \quad (1)$$

where w_{1L} is the 1-D spectral strength and γ_{1L} is the 1-D spectral exponent. These parameters are determined from regressions of the power spectra using the linearized form [15],

$$10 \log_{10} W_{1L} = 10 \log_{10} w_{1L} - \gamma_{1L} 10 \log_{10} k, \quad (2)$$

where the base 10 logarithm has been used to express the spectral level and spectral strength in dB. The parameters determined from the best fit to the mean roughness power spectrum at

each site are given in Table II along with their associated uncertainties. These uncertainties can be used to estimate the 95% confidence levels, details of which are discussed in Appendix A. Examples of the power-law fits and associated 95% confidence limits are shown in Figure 5.

In the example fits, S7 and S4 are well approximated by the power-law model spectrum. As discussed in the previous section, several sites showed the presence of anisotropic ripple and at the S1 site, the IMP2 was aligned such that the ridges of the ripple were perpendicular to the length of the IMP2. This resulted in a strong peak in the spectrum at $k = 20$ rad/m which corresponds to a ripple wavelength of 31 cm. While the wavenumber for the ripple sits squarely within the low-wavenumber region, diver observations and video indicate that the ripple is aligned such that its ridges are parallel to the reverberation track and as a result, it should have little effect on backscattering. It does, however, make it difficult to measure the isotropic component of the roughness at the site, since the ripple dominates the spectra over a significant portion of the low-wavenumber region. An alternative approach would be to model the spectrum as the combination of a ripple component and an isotropic component, however the limited number of spectral values within the low-wavenumber region makes it difficult to have confidence in the output of this approach. Instead, an isotropic spectrum is assumed and this causes the model to likely overestimate the spectral parameters, which degrades the quality of the fit as reflected in the uncertainties for the spectral parameters in Table II. Site T3 also shows evidence of anisotropy but it is difficult to discern the cause from the DEM.

As discussed in the previous section, more 1-D spectra are available in the cross-track direction and the mean spectra are consequently less noisy. As a result, the cross-track spectra are used for the model fits in the high-wavenumber region. In this region, the roughness power spectrum is also modeled as a power-law,

$$W_{1H}(k) = \frac{w_{1H}}{k^{\gamma_{1H}}}, \quad (3)$$

and the 95% confidence levels for the model fit are determined using the uncertainties in the spectral parameters for the high-wavenumber region, $\sigma_{w_{1H}}$ and $\sigma_{\gamma_{1H}}$. Examples of these fits are also shown in Figure 5 and the spectral parameters and uncertainties are given in Table II.

From the overview in Figure 3 and the examples in Figure 5, it is clear that all of the spectra in this region are very well approximated by a power-law fit. This is reflected in the uncertainties

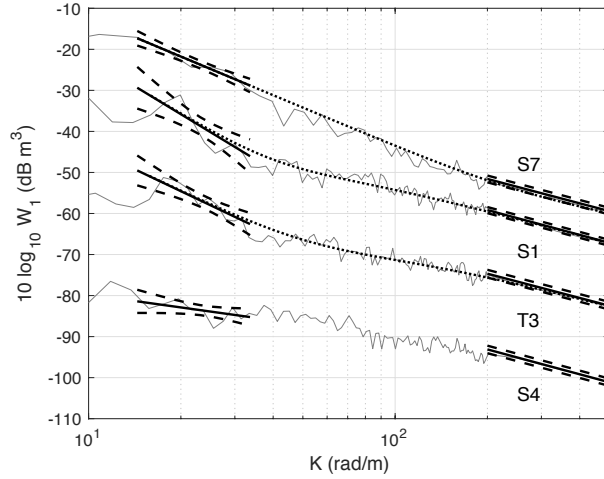


Fig. 5. Example spectra with fits to the low-wavenumber (14.4–33.6 rad/m), high-wavenumber (200–2500 rad/m), and mid-wavenumber (33.6–200 rad/m) regions. For clarity, the spectra have been offset from one another by 15 dB. Site T3 has no offset applied. The low- and high-wavenumber power-law spectra are shown as the black lines in the appropriate regions while the 95% confidence limits for those fits are shown as dashed lines. The full spectrum model, Eq. 4, is shown for sites T3, S1, and S7 as the dotted line. As discussed in Sec. II, above the 200 rad/m the spectra were determined from the cross-track roughness profiles while below 200 rad/m, the spectra were determined from along-track profiles.

in the spectral parameters which are two orders of magnitude smaller than those in the low-wavenumber region. While the spectral exponents in the low-wavenumber region vary between 1.04 and 4.53, the spectral exponents in the high-wavenumber region are tightly clustered about the mean value of $\langle \gamma_{1H} \rangle = 1.96$.

For all but two of the measured 1-D power spectra, the mid-wavenumber spectral region can be modeled by approximating the entire spectrum as the sum of two spectra,

$$W_1(k) = W_{1L}(k) + W_{1H}^v(k), \quad (4)$$

where W_{1L} is the low-wavenumber power-law spectrum given by Eq. 3, and

$$W_{1H}^v(k) = \frac{w_{1H}}{(k^2 + (1/L)^2)^{\gamma_{1H}/2}}, \quad (5)$$

is a von Karman spectrum which uses the spectral parameters w_{1H} and γ_{1H} determined from the power-law fits in the high-wavenumber region, and L is an additional parameter that determines

TABLE III

THE 2D SPECTRAL PARAMETERS FOR THE LOW- AND HIGH-WAVENUMBER REGIONS AT EACH SITE. THESE PARAMETERS WERE FOUND USING THE PARAMETERS IN TABLE II AND Eqs. 7 AND 8. THE UNCERTAINTIES WERE FOUND BY PROPAGATING THE UNCERTAINTIES IN THE 1-D SPECTRAL PARAMETERS THROUGH Eqs. 7 AND 8.

Site	Low-wavenumber Power-Law Parameters (14.4–33.6 rad/m)				High-wavenumber Power-Law Parameters (200–2500 rad/m)			
	γ_{2L}	w_{2L} ($\times 10^3$ m $^{4-\gamma_{2L}}$)	$\sigma_{\gamma_{2L}}$	$\sigma_{w_{2L}}$ (dB m $^{4-\gamma_{2L}}$)	γ_{2H}	w_{2H} ($\times 10^3$ m $^{4-\gamma_{2H}}$)	$\sigma_{\gamma_{2H}}$	$\sigma_{w_{2H}}$ (dB m $^{4-\gamma_{2H}}$)
T1	4.27	1.9219	0.846	11.571	3.01	0.0054	0.007	0.228
T2	2.14	0.0005	0.501	6.826	2.96	0.0071	0.009	0.262
T3	4.55	3.2349	0.751	10.378	2.96	0.0175	0.015	0.460
T4	3.89	0.4271	0.557	7.583	2.97	0.0173	0.013	0.410
T5	3.72	0.4665	1.378	18.851	2.79	0.0013	0.021	0.656
T6	5.24	39.7579	0.528	7.217	2.92	0.0053	0.018	0.542
T7	4.47	2.7656	0.955	13.057	2.90	0.0196	0.019	0.586
S1	5.53	166.0926	1.101	15.097	3.01	0.0253	0.012	0.362
S2	4.64	5.3137	1.019	14.033	3.01	0.0233	0.009	0.288
S3	4.73	5.6463	0.666	9.200	3.02	0.0281	0.014	0.428
S4	2.04	0.0004	0.581	8.035	3.01	0.1056	0.014	0.444
S6	3.87	0.7492	0.690	9.472	2.87	0.0023	0.009	0.282
S7	4.13	1.6310	0.387	5.262	2.97	0.0038	0.013	0.402
S8	4.53	8.8596	0.694	9.615	3.02	0.0080	0.011	0.339

the scale at which the spectrum transitions between the high- and low-wavenumbers regimes. This combined spectrum is applicable if $\gamma_{1L} > \gamma_{1H}$ and $w_{1L} > w_{1H}$, in which case $W_{1L} < W_{1H}^v$ in the high-wavenumber region. If this condition is not true, as in the case of site T2 and S4, W_{1L} will dominate the entire spectrum and overestimate the spectral strength in both the mid-wavenumber and high-wavenumber regions as can be seen in Figure 5. As a result, we will

exclude these two spectra from the subsequent analysis. For these cases, a separate model would be required in the mid-wavenumber region and the 2-D spectrum would then be found from application of Eq. D.20 in [1].

To fit the model spectrum given by Eqs. 4 and 5, the value of L given in Table II is found numerically by minimizing the error between the model spectrum and the measured spectrum across all three wavenumber regions. Examples of this combined spectrum are also shown in Figure 5. No effort has been made to estimate the uncertainties associated with L or the combined fit in general. For the examples in Figure 5, while the combined model captures the spectral behavior in the mid-wavenumber region, it does produce slight deviations from the pure power-law behavior in the high- and low-regions. These deviations are generally less than 0.5 dB with the exceptions being sites S2 and S3 where the deviation at $k = 33.6$ rad/m is 2–3 dB.

Having established a 1-D power-law spectrum and von Karman spectrum for each of the three wavenumber regions of interest, the 1-D spectra can be related to the corresponding 2-D spectra with the assumption of isotropy using

$$W_1(k_x) = \int W_2(k_x, k_y) dk_y. \quad (6)$$

With this expression and the assumption of anisotropy, the 1-D spectral parameters can be related to those in the 2-D spectra:

$$\gamma_2 = \gamma_1 + 1, \quad (7)$$

$$w_2 = w_1 \frac{\Gamma\left(\frac{\gamma_2}{2}\right)}{\sqrt{\pi} \Gamma\left(\frac{\gamma_2-1}{2}\right)}, \quad (8)$$

and L is the same in both 1-D and 2-D. Using these relationships, the 2-D spectral parameters are given in Table III. The uncertainties in the 1-D spectral parameters can also be propagated through Eqs. 7 and 8 to determine the uncertainties in γ_2 and w_2 . These uncertainties are given in Table III as well. In 2-D, again the spectra in the low- and high-wavenumber regions can be expressed as power-laws (Eq. 3) or the entire spectrum can be written as the sum of a power-law and a von-Karman spectrum,

$$W_2(k) = \frac{w_{2L}}{k^{\gamma_{2L}}} + \frac{w_{2H}}{(k^2 + (1/L)^2)^{\gamma_{2H}/2}}. \quad (9)$$

As before, this combined spectrum produces slight deviations from the power-law fits in the low- and high-wavenumber regions, but in the transformation from 1-D to 2-D, these deviations have been reduced. This reduction is due to the increase in the spectral exponents and the decrease in the spectral strengths. For sites S2 and S3 these deviation has been reduced by half to approximately 1.0–1.5 dB.

B. Spectral estimates using echosounder correlation

In order to determine if it is possible to leverage the MBES backscatter survey to estimate the spatial dependence of the roughness spectrum at TREX13, correlations with the backscatter levels will be sought for both the low- and high-wavenumber spectral parameters, starting first with the low-wavenumber spectra. The spectral strength and spectral exponent are plotted versus MBES backscatter level in Figure 6. A linear regression reveals a weak negative correlation between the spectral strengths and the backscatter level, however the uncertainties associated with this fit are large (≥ 10 dB) reflecting the very small correlation coefficient, $r = -0.078$. With a correlation coefficient of $r = 0.0083$, the spectral exponents are uncorrelated to the backscatter level and are distributed about the mean value of $\langle \gamma_{1L} \rangle = 3.13$ with a standard deviation of $\sigma_{\gamma_{1L}} = 0.53$.

The results in Figure 6 suggest that a fair approximation to the low-wavenumber spectra can be made by assuming that the spectral exponent is constant and equal to the mean value throughout the TREX13 site. Making this assumption, the spectral strength for each deployment location was recalculated using a linear regression where the spectral exponent was approximated by the mean exponent to each low-wavenumber spectrum (Eq. 31). The resulting spectral strengths are shown as a function of MBES backscatter level in Figure 7. While in Figure 6(a) the spectral strengths for the linear regression at each site are spread over a large range (approximately 52 dB in width), the spectral strengths found using the mean spectral exponent are much more tightly clustered and fall within a 7 dB range. While the variance in the spectral strength given by Eq. 32 includes both the variance of the spectral levels about the fit and the variance associated with the mean spectral exponent, the errorbars for the spectral strengths in Fig. 7 do not include the variance associated with the mean spectral exponent. An error in the mean spectral exponent

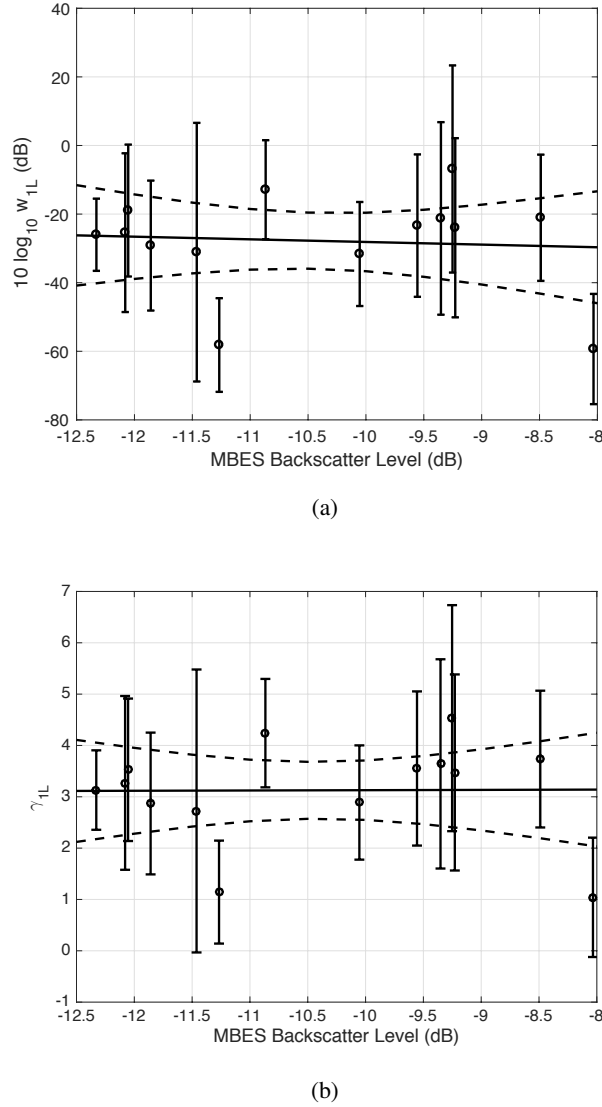


Fig. 6. The (a) 1-D spectral strengths and (b) spectral exponent given in Table II for the low-wavenumber region as a function of 400 kHz MBES Backscatter Level. The black lines in each panel are linear regressions to the data while the dashed lines are the uncertainties associated with the fits.

would manifest in an identical shift of the all the spectral strengths and as a consequence does not affect the correlation in Fig. 7.

While there was an indication of a negative relationship between the spectral strengths and backscatter level in Figure 6(a), this relationship is much more pronounced when the mean exponent is used ($r = -0.704$). For this case, the relationship between the spectral strength and the backscatter level can be expressed as

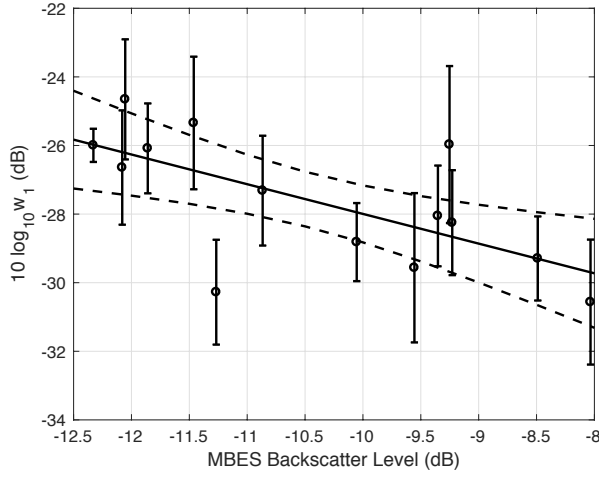


Fig. 7. The low-wavenumber, 1-D spectral strengths as a function of backscatter level when $\langle \gamma_{1L} \rangle$ is used for the spectral exponent. The solid line is the linear fit to the data while the dashed lines show the uncertainty in the fit.

$$10 \log_{10} w'_{1L} = A_{1L} + B_L S_{mb}, \quad (10)$$

where $A_{1L} = -36.7$ dB, $B_L = -0.87$, and S_{mb} is the 400 kHz MBES backscattering level.

The final approximation in the low-wavenumber region can now be written as

$$W_{1L} = \frac{w'_{1L}}{k \langle \gamma_{1L} \rangle}, \quad (11)$$

where w'_{1L} can be found from Eq. 10, $\langle \gamma_{1L} \rangle = 3.13$, and the uncertainty in the spectral levels can be approximated by the confidence interval defined by $I_{0.95}(W_{1L}) = W_{1L}(1 + \delta w_{1L})$ where $\delta w_{1L} = [-0.330, 0.492]$ and which incorporates the full variance given by Eq. 32.

Examples of these approximate spectra are shown in Figure 8 for the same SLS deployment locations shown in Figure 5. As expected, the approximate spectra do not capture the measured results as well as the previous fits, but they do capture the overall trends and spectral levels. Note that in using the mean spectral exponent, several of the measured spectra will be poorly modeled since they fall well away from the mean as can be seen in Figure 6b. One of these spectra, Site S4 which is shown in Figure 8, had a spectral exponent of $\gamma_{1L} = 1.04$ and the disagreement between the measured and approximate spectra is evident. It is reasonable that these

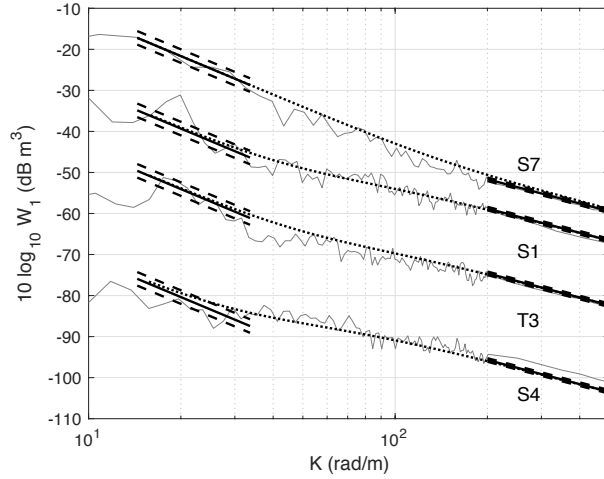


Fig. 8. Example spectra with approximate fits to the low-wavenumber (14.4–33.6 rad/m), high-wavenumber (200–2500 rad/m), and mid-wavenumber (33.6–200 rad/m) regions. For clarity, the spectra have been offset from one another by 15 dB. Site T3 has no offset applied. The low- and high-wavenumber power-law spectra are shown as the black lines in the appropriate regions while the approximate 95% confidence limits for those fits are shown as dashed lines. The full spectrum model, Eq. 18, is shown for sites T3, S1, and S7 as the dotted line.

discrepancies should follow from the statistics of independent spectral measurements, however, since only 14 independent measurements were made using this system at the TREX13 site, it is difficult to be certain that these are simply statistical variations or whether these sites should be treated as outliers where the roughness-generated mechanism differs from the other sites. A second set of roughness data was also collected during the experiment [16] and future work will look to verify this approximate approach using that dataset.

Using this approach, the two-dimensional power spectrum can also be approximated, assuming isotropy, as

$$W_{2L} = \frac{w'_{2L}}{k \langle \gamma_{2L} \rangle}, \quad (12)$$

where $\langle \gamma_{2L} \rangle = 4.13$, the spectral strength is

$$10 \log_{10} w'_{2L} = A_{2L} + B_L S_{mb}, \quad (13)$$

where $A_{2L} = -37.93$ dB, B_L is the same value as used for the 1D spectrum (Eq. 10), and the 95% confidence levels can be approximated as $I_{0.95}(W_{2L}) = W_{2L}(1 + \delta w_{1L})$.

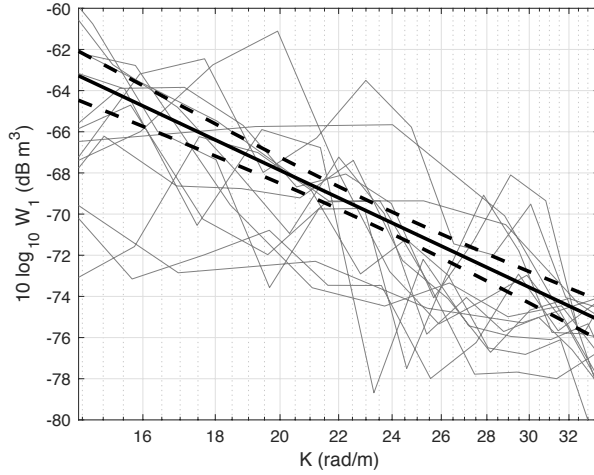


Fig. 9. The 1-D power-law roughness spectrum for the low-wavenumber region (black line) determined from the mean of the spectra measured at each site (gray lines). The 95% confidence limits for the power-law spectrum are shown as the dashed lines.

TABLE IV

THE 1D AND 2D SPECTRAL PARAMETERS FOR THE POWER-LAW FIT TO THE MEAN OF THE SPECTRA IN THE LOW-WAVENUMBER REGION MEASURED FROM ALL SITES AT TREX13.

Parameter	Value
γ_{1Lm}	3.23
w_{1Lm}	$0.0026 \text{ m}^{3-\gamma_{1Lm}}$
$\sigma_{\gamma_{1Lm}}$	0.254
$\sigma_{w_{1Lm}}$	$3.4815 \text{ dB m}^{3-\gamma_{1Lm}}$
δ_{1Lm}	$[-0.155, 0.183]$
γ_{2Lm}	4.23
w_{2Lm}	$0.0015 \text{ m}^{4-\gamma_{2Lm}}$

The validity of these spatially-dependent spectral parameters rests on the correlation in Fig. 7 which, with a correlation coefficient of $r = -0.704$, might not be make not make a convincing case for this approach. The alternative interpretation is that the spatially variability of the spectra in the low-wavenumber region is entirely random and the most appropriate approach is to simply

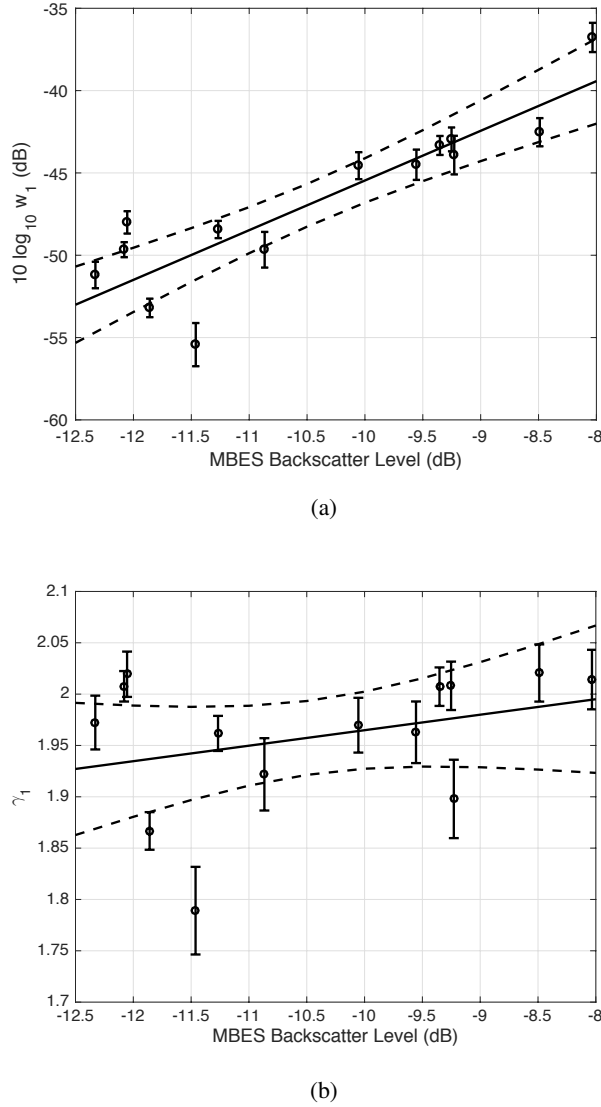


Fig. 10. The (a) 1-D spectral strengths and (b) spectral exponents given in Table II for the high-wavenumber region as a function of 400 kHz MBES backscatter level. The black lines in each panel are linear regressions to the data while the dashed lines are the 95% confidence intervals associated with the fits.

consider a power-law fit to the mean of the measured spectra as shown in Fig. 9. The parameters for the power-law fit in Fig. 9 are given in Table IV. As before, the 95% confidence limits for this fit can be approximated as $I_{0.95}(W_{1Lm}) = W_{1Lm}(1 + \delta w_{1Lm})$. With the assumption of isotropy, the corresponding 2-D spectral parameters are also given Table IV and the 95% confidence limits can also be approximated by $I_{0.95}(W_{2Lm}) = W_{2Lm}(1 + \delta w_{1Lm})$. A comparison of the spectral levels produced by both approaches is given Section IV.

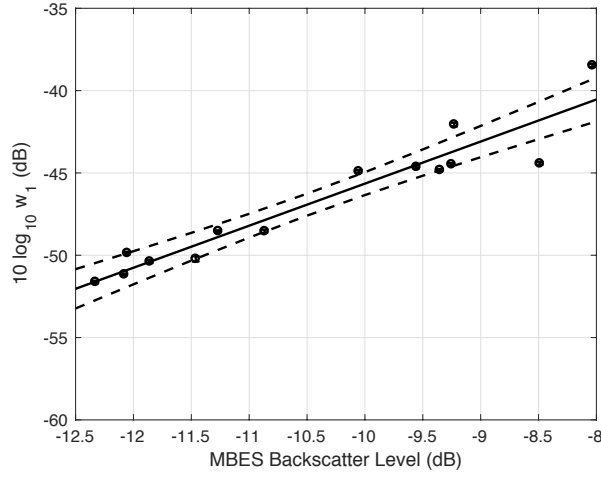


Fig. 11. The high-wavenumber, 1-D spectral strengths as a function of backscatter level when $\langle \gamma_{1H} \rangle$ is used for the spectral exponent. The solid line is the linear fit to the data while the dashed lines show the uncertainty in the fit.

For the high-wavenumber region, a similar comparison of the spectral strengths and spectral exponents to the MBES backscatter level is made in Figure 10. In this case, there is a very pronounced correlation between the spectral strength and the backscatter level ($r = 0.883$) while the correlation for the spectral exponent is much weaker ($r = 0.321$). This weak correlation for the spectral exponent again suggests that the spectral exponent could be well-approximated across all of the locations by the mean value, $\langle \gamma_{1H} \rangle = 1.96$, which has a standard deviation, $\sigma_{\langle \gamma_{1H} \rangle} = 0.0182$, that is an order of magnitude smaller than that found for the low-wavenumber region.

Using the mean spectral exponent, the spectral strengths were again determined from a least-squares fit to the data and are shown in Figure 11. Again there is a clear correlation to the backscattering strength as was observed in Figure 10a with nearly the same linear fit, but now the spread in values about this fit is significantly reduced. This again suggests that across the TREX13 experiment site the spectral exponent can be approximated by the mean and the spectral strength can be determined from the linear relationship with the MBES backscattering level. Note that the weak linear dependence of the spectral exponent in Figure 10b could also be used, but the results are negligibly different from the results when using the mean spectral exponent. Taking this approach, the roughness power spectrum for the high-wavenumber region becomes

$$W_{1H} = \frac{w'_{1H}}{k^{\langle \gamma_{1H} \rangle}}, \quad (14)$$

where the spectral strength is determined from the linear fit in Figure 11,

$$10 \log_{10} w'_{1H} = A_{1H} + B_H S_{mb}, \quad (15)$$

where $A_{1H} = -20.10$ dB and $B_H = 2.56$. The 95% confidence interval can be approximated by $I_{0.95}(W_{1H}) = W_{1H}(1 + \delta w_{1H})$ where $\delta w_{1H} = [-0.0944, 0.1043]$.

Examples of the approximate spectrum for the high-wavenumber region are shown in Figure 8. For the examples shown here, the approximation provides a good fit to Sites S7 and T3 while underestimating S4 and overestimating S1. These misfits are a consequence of the discrepancy between the backscatter-predicted spectral strengths and the measured spectral strengths at these sites. In fact, examination of Figure 11 indicates that all of the sites with the highest 400 kHz backscattering levels are poorly approximated (S4 has the highest backscattering level while S1 has the third highest). These sites have many shells and shell fragments on the sediment interface and within the sediment. The high density of shells on the interface could be adversely affecting the SLS measurements of the roughness or the shell density in the sediment is reaching a level such that higher-order effects may be changing the backscatter response. Regardless of the cause, the 1-D spectral strengths in these high backscatter regions may be inaccurate by as much as 2 dB.

The 2-D roughness power spectrum in this region can be approximated as

$$W_{2H} = \frac{w'_{2H}}{k^{\langle \gamma_{2H} \rangle}}, \quad (16)$$

where $\langle \gamma_{2H} \rangle = 2.96$, the spectral strength is

$$10 \log_{10} w'_{2H} = A_{2H} + B_H S_{mb}, \quad (17)$$

$A_{2H} = -20.79$ dB, B_H is the same value as used for the 1D spectrum (Eq. 15), and the 95% confidence levels can be approximated as $I_{0.95}(W_{2H}) = W_{2H}(1 + \delta w_{1H})$.

To approximate the roughness power spectra over the entire wavenumber range at all locations within the TREX13 site, the results for the high and low wavenumber regions can be again combined into a single spectrum,

$$W_1(k) = W_{1L}(k, S_{mb}) + W_{1H}^v(k, S_{mb}), \quad (18)$$

where $W_{1L}(k, S_{mb})$ is the low-wavenumber power-law spectrum given by Eqs. 10 and 11,

$$W_{1H}^v(k, S_{mb}) = \frac{w'_{1H}(S_{mb})}{(k^2 + (1/L(S_{mb}))^2)^{\gamma_{1H}/2}}, \quad (19)$$

and $w'_{1H}(S_{mb})$ is given by Eq. 15 and a characteristic length, L , has been introduced to capture the transition between the high and low wavenumber spectra. As before, the characteristic length for each site can be found from a least-squares fit to the full spectrum at that site. The results of these fits are shown as a function of backscattering level in Figure 12. There is a approximate linear dependence of the characteristic length on the backscatter level which is improved if sites T2 and T4 are excluded from the fit as was done in Figure 12. The characteristic length as a function of backscatter level can be expressed as

$$L = a_L + b_L S_{mb}, \quad (20)$$

where $a_L = 0.035$ m, $b_L = 0.002$ m/dB, $\sigma_a = 0.01$ m, and $\sigma_b = 0.001$ m/dB. Using this relation in Eq. 18, the full spectral approximation is shown for the examples in Figure 8. While the uncertainties associated with L make it possible to estimate the uncertainty across the entire wavenumber range, these bounds are not shown in Figure 8 in order to retain clarity.

IV. DISCUSSION

Although the SLS was only deployed at 14 locations along the TREX13 main reverberation track, the spatial dependence of the shell content at this site made it possible to predict the spectral parameters throughout the site by exploiting the relationship between the spectral parameters and the 400 kHz backscatter measurements. It is reasonable that the roughness and backscatter should be related for the high wavenumber portion of the roughness spectrum: The high end of that wavenumber region, $k = 2500$ rad/m, corresponds to the Bragg condition for backscattering of 400 kHz sound incident on the sediment at a grazing angle of 41.75° for first-order perturbation theory. Thus much of the rough surface scattering of the incident beams is driven by the spectra for $k > 250$ rad/m.

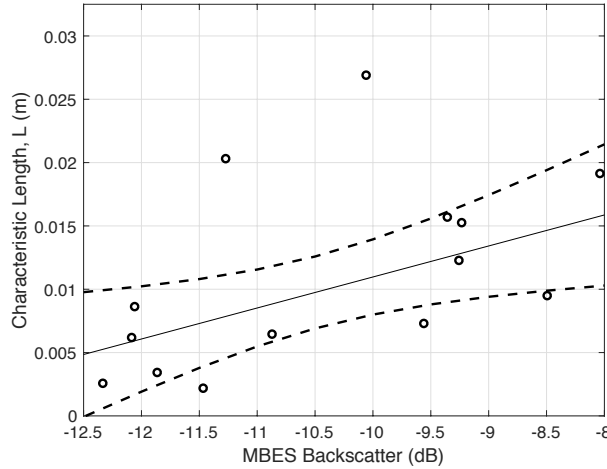
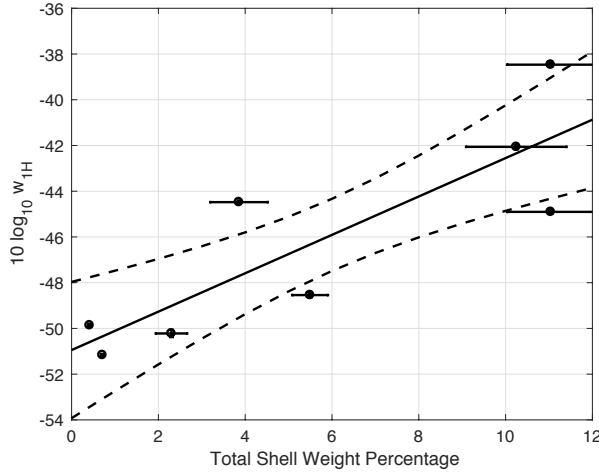
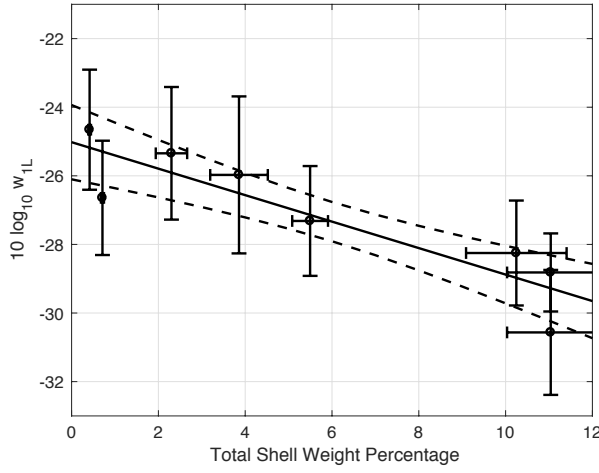


Fig. 12. The characteristic length at each measurement location determined from a least-squares fit over the full range of wavenumbers using Eq. 18 as a function of the 400 kHz multibeam backscatter. The linear fit and associated confidence limits exclude the two largest characteristic lengths.

Rough surface scattering, however, is not the dominant high-frequency scattering mechanism for steep grazing angles at the TREX13 site. Measurements of the shell content at the site indicate that the amount of shell varies, increasing from 1% to 11% of the sediment volume as one moves from the northwest to the southeast across each ridge. For sound incident above the critical grazing angle, this shell and shell hash act as discrete volume scatterers and the density of these scatterers is such that this is the dominant mechanism for high-frequency backscatter. This was shown to be the case through data/model comparisons for high-frequency backscatter at the location of the R/V Sharp and through inversions of 200–400 kHz MBES time series data[14]. So while the backscatter is correlated with the roughness, roughness is not the cause of the 400 kHz MBES backscatter. Examination of the measured surfaces indicates that the high-wavenumber roughness is predominately due to the presence of shells on the sediment interface. Grab samples collected at several of the SLS deployment locations confirm that as the shell content within the sediment increases, the high-wavenumber roughness also increases (Figure 13a). The correlation between the roughness and the backscatter is not because the roughness is the dominant scattering mechanism but instead is a consequence of the correlation between the roughness and the shell content and between the backscatter level and the shell content..



(a)



(b)

Fig. 13. Approximate spectral strengths as a function of the percentage of shell making up the total weight of the sediment for (a) the high-wavenumber and (b) the low-wavenumber portions of the spectrum.

The low-wavenumber portion of the roughness power spectrum does not contribute to rough surface scattering at 400 kHz so it comes as a surprise that there should be any kind of a correlation in this case. The explanation may again be related to the shell content of the sediment as indicated in Figure 13b where there is a clear negative correlation between the low-wavenumber spectral strength and the shell content. Examination of the measured surfaces indicate that in the low shell content areas, the low-wavenumber roughness is the result of bioturbation, predominately pock marks produced by fish foraging and burrowing in the seafloor.

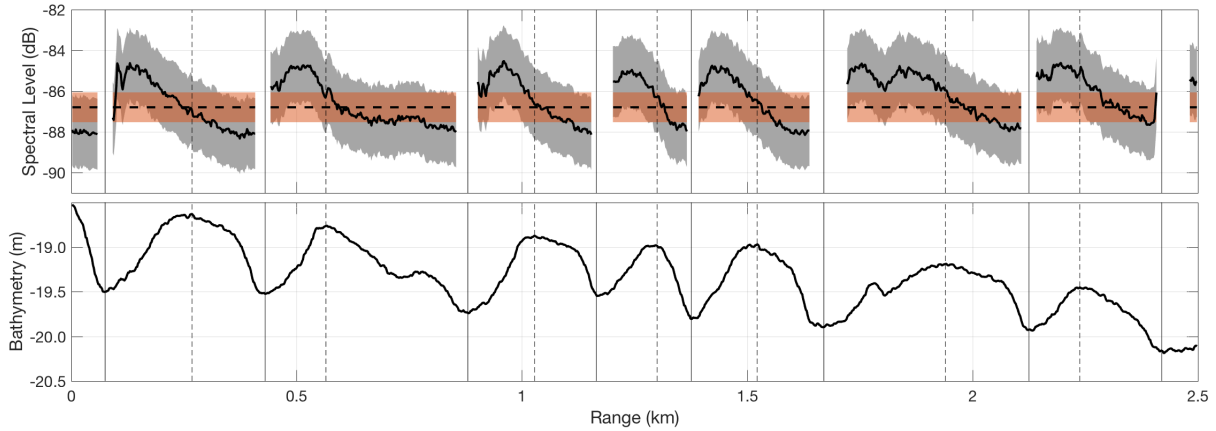


Fig. 14. (Upper Panel) The 2-D spectral level calculated using Eq. 12 along the 129° radial from the TREX13 reverberation (solid line and gray bars) and using the mean spectral parameters in Table IV (dashed line and orange bars). These spectral levels are calculated for the Bragg wavenumber corresponding to backscattering for a 3 kHz plane wave incident on the seafloor at a grazing angle of 5 degrees. The grey and orange areas correspond the range of the 95% confidence levels. (Lower Panel) The bathymetry along the same 129° radial. The solid vertical lines correspond to the position of the swales between sand ridges and the dashed lines correspond to the position of the sand ridge peaks.

In the high shell content surfaces, while the most pronounced surface features are the sand ripples discussed previously, there is a clear absence of bioturbation. A possible explanation may be that the high shell content inhibits or obscures bioturbation in these areas by either making it difficult for the fish to rework these sediments or by filling in the pock marks with shell when the sediment is disturbed. In either case, this would cause the spectral strength to be negatively correlated to the shell content and consequently to the 400 kHz backscatter as well.

Regardless of the mechanism that produces the low-wavenumber roughness, the results of the roughness measurements and their extension throughout the TREX13 site have important implications for the modeling of the 2–4 kHz reverberation measurements. The spectral exponent was found to be uncorrelated with the backscatter strength and to have a mean value of $\langle \gamma_{2L} \rangle = 4.13$. Using the roughness power spectrum in first order perturbation theory to estimate the contribution of rough surface scattering to the reverberation, this mean spectral exponent implies that there should be negligible frequency dependence to the scattering since $\sigma \approx k^4 W_{2L}(k)$. This is reflected in the reverberation data which show little to no frequency dependence over

the 2–4 kHz range [2].

Since the spectral strength throughout the experiment site is approximated as a function of the 400 kHz backscatter level, the roughness spectra, and consequently the roughness scattering, is expected to have a strong spatial dependence. Figure 14 shows the spectral strength calculated using the backscatter data along the main beam of the reverberation measurements (129° from North) for the Bragg wavenumber corresponding to backscattering for a 3 kHz plane wave incident on the seafloor at a grazing angle of 5 degrees. The predicted spectral strength fluctuates by 3 dB along this track. These fluctuations are correlated with the bathymetry and the spectral strength is highest on the northwest slopes of the sand ridges (left side of ridges in the figure) and lowest on the southeast slopes (right side of ridges in the figure). Note that in the figure, the spectral levels in the swales are not shown. While these are the location of the lowest 400 kHz backscatter levels, and consequently the highest roughness spectral levels, they also correspond to muddy regions. In the muddy regions, the IMP2 would sink into the mud and no roughness measurements could be made as a result, nor should the roughness scattering from these mud interfaces be significant. Hence they have been excluded from the figure.

Direct path measurements of backscatter along the main reverberation track indicate that while roughness may be the dominant mid-frequency scattering mechanism from the sandy regions, there is significant volume scattering contributions from the mud regions[17]. While the spatial variability of the roughness may explain the general trend of the reverberation level with range, the volume scattering from the mud regions are likely responsible for the largest fluctuations in the reverberation level.

Also shown in Figure 14 is the spectral level for the same Bragg wavenumber when the mean spectral parameters in Table IV are used. As expected, the resulting spectral level passes roughly through the middle of the range of values for the spatially dependent prediction. The maximum difference between these two predictions is approximately 2.5 dB and as a result, the mean spectral parameters may provide a acceptable approximation to the overall trend in the reverberation due to roughness scattering.

V. SUMMARY

The primary goal of TREX13 iwas to measure reverberation with sufficient environmental characterization to reduce ambiguity in the data/model comparisons. While efforts were made

to minimize the area over which environmental measurements were needed, the seafloor was such that any individual set of measurements could not capture the spatial variability of the sediment properties. In the case of sediment roughness, it was possible to combine the measurements with the more densely sampled data from the multibeam survey to develop a means of estimating the sediment roughness throughout the experiment site. This is key for modeling the reverberation measured during TREX13, since the measured reverberation shows fluctuations in the reverberation level that are correlated with the bathymetry.

APPENDIX

A. Spectral Fits and Uncertainties

The 1-D roughness power spectra can be approximated by power laws of the form,

$$W_1(k) = \frac{w_1}{k_1^\gamma}, \quad (21)$$

where w_1 is the spectral strength and γ_1 is the spectral exponent. These parameters can be determined via a linear regression when the log of the equation is taken,

$$\hat{WL}_1 = WS_1 - \gamma_1 K, \quad (22)$$

where $\hat{WL}_1 = 10 \log_{10} \hat{W}_1$ is the spectral level determined from the linear regression, $WS_1 = 10 \log_{10} w_1$, and $K = 10 \log_{10} k$. The base 10 logarithm has been used in order to express the spectral level and spectral strength in decibels.

Analyzing the spectral levels, WL_i , measured at each K_i using least squares [15], the spectral strength and spectral exponent can be calculated from

$$WS_1 = \frac{1}{N} \sum_i WL_i + \gamma_1 \langle K_i \rangle \quad (23)$$

and

$$\gamma_1 = -\frac{\sum_i WL_i (K_i - \langle K_i \rangle)}{\sum_i (K_i - \langle K_i \rangle)^2}, \quad (24)$$

where

$$\langle K_i \rangle = \frac{1}{N} \sum_i K_i \quad (25)$$

is the mean of the wavenumber band of interest.

Using the linear fit, the variance of the measured spectral levels can be estimated as

$$\sigma_{WL_1}^2 = \frac{1}{N-2} \sum_i (WL_i - WS_1 + \gamma_1 K_i)^2 \quad (26)$$

and using this expression, the variance associated with the uncertainties in the spectral strength and spectral exponent can be determined from Eq. 23 and 24,

$$\sigma_{WS_1}^2 = \sigma_{WL_1}^2 \left[\frac{1}{N} + \frac{\langle K_i \rangle^2}{\sum_i (K_i - \langle K_i \rangle)^2} \right] \quad (27)$$

and

$$\sigma_{\gamma_1}^2 = \frac{\sigma_{WL_1}^2}{\sum_i (K_i - \langle K_i \rangle)^2}. \quad (28)$$

Finally the uncertainty in the spectral fit can be expressed as

$$\begin{aligned} \sigma_{\hat{WL}_1}^2 &= \sigma_{WL_1}^2 \left[\frac{1}{N} + \frac{(K - \langle K_i \rangle)^2}{\sum_i (K_i - \langle K_i \rangle)^2} \right] \\ &= \sigma_{WS_1}^2 + (K^2 - 2K \langle K_i \rangle) \sigma_{\gamma_1}^2. \end{aligned} \quad (29)$$

Using the variance in the spectral fit, the 95% confidence interval for the linear fit can be expressed as

$$I_{0.95}(\hat{WL}_1) = WS_1 - \gamma_1 K \pm 2\sigma_{\hat{WL}_1}. \quad (30)$$

B. Spectral fits using the mean spectral exponent

In Section III-B, an alternative set of power-laws are sought where the spectral exponent at each site is approximated by the mean of the spectral exponents measured at all of the sites. In this case, least squares yields a new equation for the spectral exponent,

$$WS_1 = \frac{1}{N} \sum_i WL_i + \langle \gamma_1 \rangle \langle K_i \rangle, \quad (31)$$

where $\langle \gamma_1 \rangle$ is the mean spectral exponent. The variance of the measured spectral strength is now

$$\sigma_{WS_1}^2 = \frac{\sigma_{WL_1}^2}{N} + \sigma_{\langle \gamma_1 \rangle}^2, \quad (32)$$

where $\sigma_{WL_1}^2$ is given by Eq. 26 with γ_1 replaced by $\langle \gamma_1 \rangle$ and $\sigma_{\langle \gamma_1 \rangle}$ is the standard deviation of the mean spectral exponent.

C. Removing bias from linear regressions of log-transformed data

One of the underlying assumptions behind the linear regressions outlined above is that the uncertainties in the spectral levels are normally distributed. While this may be true for WL_1 , it is not true for $10 \log_{10} WL_1$ and the means in Eq. 23 and 24 will be biased leading to an

underestimation of the spectral strength and spectral exponent. While in many cases this bias may be small, an analysis of this bias and a technique to remove it are given here.

We assume that the spectra, WL_1 , is described by a combination of a power-law, $W_1(k_i) = w_1 k_i^{-\gamma_1}$, and a random fluctuation, δ_i , which is normally distributed with $\langle \delta_i \rangle = 0$,

$$WL_1(k_i) = W_1(k_i) + \delta_i. \quad (33)$$

In order to use linear regression, we apply $10 \log_{10}$ to both sides of the equation and, to facilitate the analysis, we rewrite the resulting expression using $10 \log_{10}(x) = 10 \ln(x) / \ln(10)$,

$$10 \log_{10} WL_1(k_i) = 4.34 \ln(W_1(k_i) + \delta_i). \quad (34)$$

We will assume that $\delta_i \ll W_1(k_i)$ and using the first two terms of the Taylor series expansion for $\ln(1 + x)$, approximate the equation as

$$10 \log_{10} WL_1(k_i) = 10 \log_{10} W_1(k_i) + \frac{\delta_i}{W_1(k_i)} - \frac{1}{2} \frac{\delta_i^2}{W_1(k_i)^2}. \quad (35)$$

If $\delta_i = 0$, linear regression applied to this equation will return W_1 without any bias. The spectral strength in Eq. 23, however, requires the mean of the $\hat{WL}_i = 10 \log_{10} WL_1(k_i)$ and, with the approximation in Eq. 35, results in a biased estimate of the spectral strength,

$$WS_{1b} = WS_1 - \frac{1}{2} \left\langle \frac{\delta_i^2}{W_1(k_i)^2} \right\rangle. \quad (36)$$

A similar approach can also be used to find the biased spectral slope,

$$\gamma_{1b} = \gamma_1 + \frac{\sum_i \left(\frac{\delta_i}{W_1(k_i)} - \frac{1}{2} \frac{\delta_i^2}{W_1(k_i)^2} \right) (K_i - \langle K_i \rangle)}{\sum_i (K_i - \langle K_i \rangle)^2}. \quad (37)$$

At first glance it would appear that the bias term for the spectral slope should be zero and this would be the case if K_i was uniformly sampled. However, since k_i is uniformly sampled and $K_i = 10 \log_{10} k_i$, the difference $\Delta K_i = K_i - K_{i-1}$ decreases with increasing K_i . As a result there are more samples for which $K_i > \langle K_i \rangle$ and the bias term is nonzero. However in both simulations and the spectra examined here, this bias term is very small with $\gamma_{1b} - \gamma_1 < 0.01$. As a consequence, the bias in the slope has been neglected in the spectral fits in this paper.

The amount of bias in the spectral strength can be estimated by considering the difference between the spectral levels and the biased power-law found via linear regression,

$$\Delta_i = 10 \log_{10} WL_1(k_i) - 10 \log_{10} W_{1b}(k_i), \quad (38)$$

where $10 \log_{10} W_{1b}(k_i) = WS_{1b} - \gamma_1 K_i$. Using Eq. 33 and 36, the difference becomes

$$\Delta_i = 10 \log_{10} (W_1(k_i) + \delta_i) - 10 \log_{10} W_1(k_i) \quad (39)$$

$$+ \frac{1}{2} \left\langle \frac{\delta_i^2}{W_1(k_i)^2} \right\rangle \quad (40)$$

$$= 10 \log_{10} \left(1 + \frac{\delta_i}{W_1(k_i)} \right) + \frac{1}{2} \left\langle \frac{\delta_i^2}{W_1(k_i)^2} \right\rangle \quad (41)$$

and the bias term can now be found via

$$10 \log_{10} \left\langle 10^{\frac{\Delta_i}{10}} \right\rangle = \frac{1}{2} \left\langle \frac{\delta_i^2}{W_1(k_i)^2} \right\rangle. \quad (42)$$

While the bias in the spectral strength can be reduced by averaging over many realizations thus reducing the size of δ_i , the bias can now be removed in general by using Eq. 42 to find the unbiased spectral strength,

$$W_1(k_i) = W_{1b}(k_i) + 10 \log_{10} \left\langle 10^{\frac{\Delta_i}{10}} \right\rangle. \quad (43)$$

ACKNOWLEDGMENT

This material is based upon research supported by the Office of Naval Research under Award Number N000141310040 and by the Strategic Environmental Research and Development Program under project number MR-2229. The author would like to thank the crew of the R/V Sharp for their assistance in deploying the SLS during TREX13. The author benefited from many discussions with and input from Eric Thorsos and Dajun Tang.

REFERENCES

- [1] D. R. Jackson and M. Richardson, *High-Frequency Seafloor Acoustics*. New York, NY: Springer, 2007.
- [2] J. Yang, D. Tang, B. T. Hefner, K. L. Williams, and J. R. Preston, “Reverberation Measurements at TREX13,” *In preparation for the IEEE J. Ocean. Eng.*, 2017.
- [3] C. P. de Moustier and B. Kraft, “400 kHz multibeam measurements at TREX13,” *In preparation for the IEEE J. Ocean. Eng.*, 2017.
- [4] K. S. Davis, N. C. Slowey, I. H. Stender, H. Fiedler, W. R. Bryant, and G. Fechner, “Acoustic backscatter and sediment textural properties of inner shelf sands, northeastern Gulf of Mexico,” *Geo-Mar. Lett.*, vol. 16, no. 3, pp. 273–278, 1996.
- [5] D. R. Jackson, K. B. Briggs, K. L. Williams, and M. Richardson, “Tests of models for high-frequency seafloor backscatter,” *IEEE J. Ocean. Eng.*, vol. 21, no. 4, pp. 458–470, 1996.

- [6] M. Richardson, K. B. Briggs, L. D. Bibee, P. Jumars, W. Sawyer, D. B. Albert, R. H. Bennett, T. K. Berger, M. J. Buckingham, N. P. Chotiros, P. H. Dahl, N. T. Dewitt, P. Fleischer, R. Flood, C. Greenlaw, D. Holliday, M. Hulbert, M. Hutnak, P. Jackson, J. Jaffe, H. Johnson, D. Lavoie, A. Lyons, C. Martens, D. McGehee, K. Moore, T. H. Orsi, J. Piper, R. Ray, A. Reed, R. Self, J. Schmidt, S. Schock, F. Simonet, R. Stoll, D. Tang, D. Thistle, E. I. Thorsos, D. Walter, and R. Wheatcroft, "Overview of SAX99: environmental considerations," *IEEE J. Ocean. Eng.*, vol. 26, no. 1, pp. 26–53, 2001.
- [7] E. I. Thorsos, K. L. Williams, N. P. Chotiros, J. T. Christoff, K. W. Commander, C. Greenlaw, D. Holliday, D. R. Jackson, J. Lopes, D. McGehee, J. Piper, M. Richardson, and D. Tang, "An overview of SAX99: acoustic measurements," *IEEE J. Ocean. Eng.*, vol. 26, no. 1, pp. 4–25, 2001.
- [8] K. L. Williams, D. R. Jackson, D. Tang, K. B. Briggs, and E. I. Thorsos, "Acoustic Backscattering From a Sand and a Sand/Mud Environment: Experiments and Data/Model Comparisons," *IEEE J. Ocean. Eng.*, vol. 34, no. 4, pp. 388–398, 2009.
- [9] K. L. Williams, D. R. Jackson, E. I. Thorsos, D. Tang, and K. B. Briggs, "Acoustic backscattering experiments in a well characterized sand sediment: data/model comparisons using sediment fluid and Biot models," *IEEE J. Ocean. Eng.*, vol. 27, no. 3, pp. 376–387, 2002.
- [10] C.-C. Wang and D. Tang, "Seafloor Roughness Measured by a Laser Line Scanner and a Conductivity Probe," *IEEE J. Ocean. Eng.*, vol. 34, pp. 459–465, 2009.
- [11] C.-C. Wang, B. T. Hefner, and D. Tang, "Evaluation of Laser Scanning and Stereo Photography Roughness Measurement Systems Using a Realistic Model Seabed Surface," *IEEE J. Ocean. Eng.*, vol. 34, no. 4, pp. 466–475, 2009.
- [12] D. Tang, "Fine-scale measurements of sediment roughness and subbottom variability," *IEEE J. Ocean. Eng.*, vol. 29, pp. 929–939, 2005.
- [13] C.-C. Wang and C. Min-Shine, "Nonmetric Camera Calibration for Underwater Laser Scanning System," *IEEE J. Ocean. Eng.*, vol. 32, no. 2, pp. 383–399, 2007.
- [14] B. T. Hefner, "Inversion of High Frequency Acoustic Data for Sediment Properties Needed for the Detection and Classification of UXO's (Final Report for MR-2229)," 2015, available at <https://serdp-estcp.org/content/download/34593/333838/file/MR-2229-FR.pdf>.
- [15] I. Guttman, *Linear models: an introduction*, ser. Wiley series in probability and mathematical statistics. Wiley, 1982.
- [16] N. P. Chotiros, M. J. Isakson, J. N. Piper, and A. McNeese, "Sea floor roughness measured by a laser profiler on a ROV," in *OCEANS 2014 - TAIPEI*. IEEE, 2014, pp. 1–4.
- [17] D. Tang, B. T. Hefner, and D. R. Jackson, "Direct-path backscatter measurements along the main reverberation track of TREX13," *In preparation for the IEEE J. Ocean. Eng.*, 2017.



Brian T. Hefner received the B.S. degree in physics from Bard College, Annandale-On-Hudson, NY, in 1994 and the M.S. and Ph.D. degrees in physics from Washington State University, Pullman, in 1996 and 2000, respectively.

From 2000 to 2001, he was a Postdoctoral Scholar at Crocker Nuclear Laboratory, University of California, Davis, where he studied light scattering from airborne dust using light detection and ranging (LIDAR). In 2001, he moved to the Applied Physics Laboratory, University of Washington, Seattle, where he is currently a Principal Physicist in the Acoustics Department. His primary research interests include acoustic interaction with the sea bottom, propagation and reverberation in shallow water, and sediment acoustics.

Dr. Hefner is a member of the Acoustical Society of America. He received the A.B. Wood Medal from the Institute of Acoustics (U.K.), with the recommendation of the Acoustical Society of America, in 2013. He was Co-Chief Scientist for the 2013 Target and Reverberation Experiment (TREX13).

High-frequency sound speed and attenuation measurements in sandy sediments with a portable velocimeter

Xavier Demoulin, Laurent Guillon, and Brian T. Hefner,

Abstract

As part of the environmental characterization at the Target and Reverberation Experiment in the Spring of 2013 (TREX13), a high-frequency acoustic array called the INvestigation of SEdiments by Acoustics (INSEA) was deployed to measure sediment sound speed and attenuation between 70 kHz and 375 kHz. This array is diver-portable and was deployed from a small boat at 5 locations along the 5 km long, main reverberation track at 20 m water depth. In addition to the acoustic measurements, sediment samples were also collected at each location and were analyzed for grain size distribution, shell content, bulk density, and porosity. In this paper, the INSEA velocimeter is presented with an analysis of the processing used to obtain the compressional sound speed and attenuation coefficient. The results from the TREX13 site in the 150 kHz to 300 kHz frequency range show a clear spatial dependence of the sediment sound speed and attenuation, with a negative sound speed dispersion that increases with increasing shell content within the sediment.

Index Terms

Underwater acoustic measurements, Acoustic propagation, Sediments

Xavier Demoulin is with Maree company, 15 rue Galilee, 56270 Ploemeur France, e-mail: xdemoulin@maree.fr

L. Guillon is with the Research Institute of the French Naval Academy, BCRM Brest CC 600 29240 Brest Cedex 9 France, e-mail: laurent.guillon@ecole-navale.fr

Brian T. Hefner is with the Applied Physics Laboratory, University of Washington, 1013 NE 40th Street, Seattle, Washington 98105, USA, e-mail: hefner@apl.washington.edu

Preliminary results on this subject were presented at the 166th Meeting of the Acoustical Society of America, December 2013, San Francisco, CA.

High-frequency sound speed and attenuation measurements in sandy sediments with a portable velocimeter

I. INTRODUCTION

The seafloor has a significant impact on sonar performance particularly in shallow-water areas where the acoustic signal can interact many times with the seafloor over a relatively short distance. Whereas seafloor roughness and volume heterogeneity strongly influence reverberation, acoustic parameters such as the sediment sound speed, attenuation, and bulk density play a significant role in both transmission loss and reverberation. In naval SONAR applications, knowledge of these parameters for a given location typically rely on acoustic databases that relate indirect measurements of bottom loss to properties such as grain size or sediment type. These databases can be problematic for sediments where the relationships between the acoustic and geological parameters are ambiguous or where the sediment type and structure is changing over relatively short distances.

Geoacoustic relationships can also be derived from theoretical models: the two most common being the Biot-Stoll model [1], which treats the sediment as a visco-porous medium, and the Grain Shearing model [2], where the sediment is treated as a granular medium. Each of these theories necessitate the knowledge of many physical parameters (porosity, elastic moduli, permeability, etc). From these theories, reflection and backscattering coefficients can be computed and then used in a propagation or reverberation code. A drawback of these theoretical approaches is that they do not take into account the complexity of the seafloor and the presence of heterogeneities that can be abundant in very shallow water. Consequently, it is important to be able to acquire direct measurements of acoustic data in such environments. A number of systems have been developed for this purpose. These include the In Situ Sound Speed and Attenuation Probe (ISSAP) developed at the University of New Hampshire [3], the In Situ Sediment geoAcoustic Measurement System (ISSAMS) at NRL-Stennis [4], and the Sediment Acoustics Measurement System (SAMS) at APL-UW [5]. Unfortunately these systems can be cumbersome to deploy

and, with the exception of SAMS, are no longer actively maintained.

To support the collection of sediment ground-truth acoustic data, a portable velocimeter named INSEA (for INvestigation of SEdiments by Acoustics) was developed recently through a collaboration of French companies and research laboratories. This velocimeter is light enough to be used by a single diver and measures sound speed and attenuation between 90 kHz and 375 kHz. In spring 2013, this velocimeter was used during TREX13 (Target and Reverberation Experiment 2013) off shore of Panama City, Florida, USA, for two objectives: first, to demonstrate its efficacy and second, to acquire data that can be compared to other acoustic data collected during the experiment.

While the INSEA makes measurements at frequencies well above the 2–4 kHz range at which the reverberation and transmission loss measurements were collected during TREX13, the INSEA data can be combined with similar data collected at 1–10 kHz by SAMS. The resulting broadband datasets provide a means of testing theories of sediment propagation and identifying the physical mechanisms that affect propagation.

In addition to measuring sound speed and attenuation with the INSEA, grab samples were collected at each of the measurement sites to determine additional sediment properties such as grain size, shell content, and porosity. After describing the operation of the INSEA and the data processing used to extract the sediment sound speed and attenuation in Section II, the acoustic and geological data collected during TREX13 are presented in Section III. In Section IV, these data are analyzed.

II. INSEA VELOCIMETER DESCRIPTION

A. INSEA

CARASEDIM, which is the acronym for CARactérisation Acoustique des SÉDIMents (acoustical characterization of sediments), was a project that French companies and research laboratories jointly conducted with the objective of studying the geoacoustic properties of sandy sediments, including coarse ones. It lasted from December 2010 to May 2013 and was funded by DGA (Délégation Générale de l'Armement). To characterize these types of sediments, the INSEA velocimeter prototype was designed and developed, and later commercialized by RTSYS company[6]. Tank and beach experiments were performed between 2011 and 2012 [7], [8]. The first sea trials with divers were conducted in France during summer 2012 [9].

The INSEA velocimeter was designed with the major objective of having a device that is very easy to use in the laboratory for tank measurements and at sea by a single diver. A common way to estimate sound speed in sediments is to measure time-of-flight between distant piezoelectric transducers (cf. [10] and references therein). This is often done in the laboratory with ultrasound probes [11] to evaluate geoacoustic models, generally using well-sorted and fine sediment [12]. The purpose of the INSEA is to use this time-of-flight method to measure in situ sound speed and attenuation for ocean sediments. Due to the heterogeneous nature of shallow water sediments, the signal processing required careful attention. Details are provided in sections II-B and II-C.

The INSEA velocimeter is suitable for shallow-water applications down to 100 m water depth. It consists of a pressure case that contains electronics and batteries for autonomous, diver operation, and four stakes, two for the sources and two for the receivers (Fig. 1). The horizontal distance between two opposite stakes can be manually adjusted from 5 to 40 cm and the depth of the transducers can be adjusted from 5 to 15 cm. During TREX13 experiment, the transducer depth was fixed at 10 cm. The horizontal distances with the two receivers were 12 cm and 18 cm for T1 and 10 cm and 14 cm for T2. We did not change this configuration during the experiment in order to be able to compare results obtained at different sites. This design allows users to study, for instance, the variations of acoustic parameters with depth.

The four transducers are devoted to compressional wave measurements. They are broadband, piezoelectric, spherical transducers cast in a resin in the middle of the cylindrical stakes. The two sources operate in two different frequency bands: transducer T1 between 70 kHz and 130 kHz and transducer T2 between 125 kHz and 375 kHz. For some of the data collected during TREX13, we observed low signal-to-noise ratios at low or high frequencies that appeared to be due, for instance, to scattering by heterogeneities. This greatly increased the uncertainties in the results at these frequencies. In order to facilitate the comparisons of sound speed and attenuation for different TREX13 sites, we've chosen to only present results in the 150 kHz to 300 kHz band.

The INSEA velocimeter can be used in two different modes. For laboratory measurements, it can be connected directly to a computer using a single cable that provides power and transfers data via ethernet. For autonomous measurements, a suite of transmission signals is uploaded to the INSEA prior to deployment. During the deployment, the diver drives the stakes into the seafloor and pushes a button that initiates data collection (Fig. 2). When the transmit-receive cycle has completed, the diver is notified and the INSEA can be removed. In practice, the diver

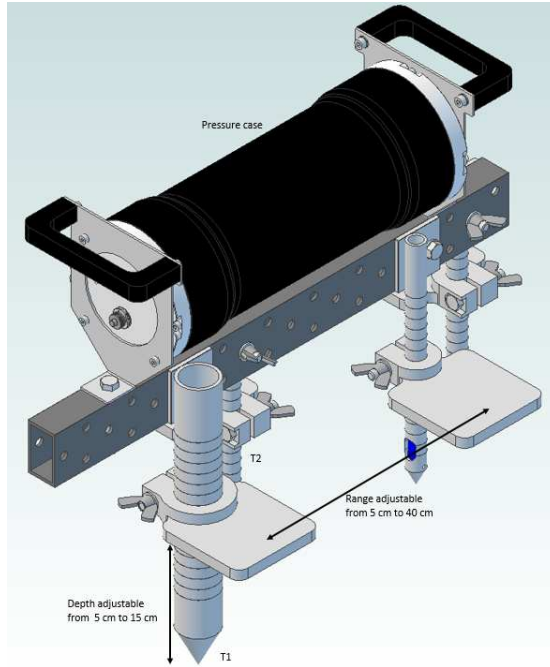


Fig. 1. Sketch of the INSEA velocimeter. The black pressure case contains the electronic card and batteries, the 4 stakes hold two sources and two receivers. The total length is 50 cm.

will insert the INSEA multiple times into the sediment, typically within a 1 m² area, in order to get sufficient statistics on the acoustic response of the seafloor. Once the diver and the device have returned to the ship, the recorded data can be downloaded to a computer via the ethernet connection.

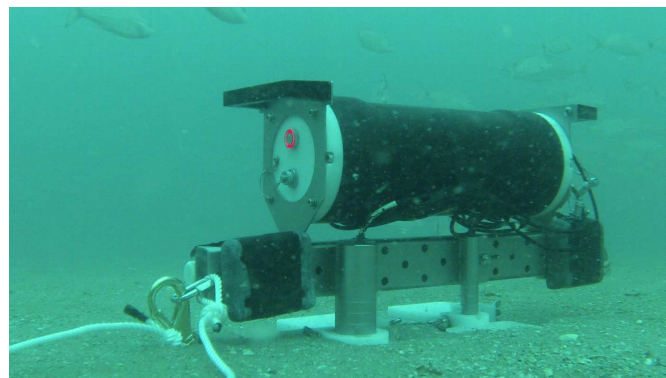


Fig. 2. INSEA velocimeter making measurements in sandy seafloor (photo courtesy of Ben Brand, APL-UW).

B. Sound speed measurements

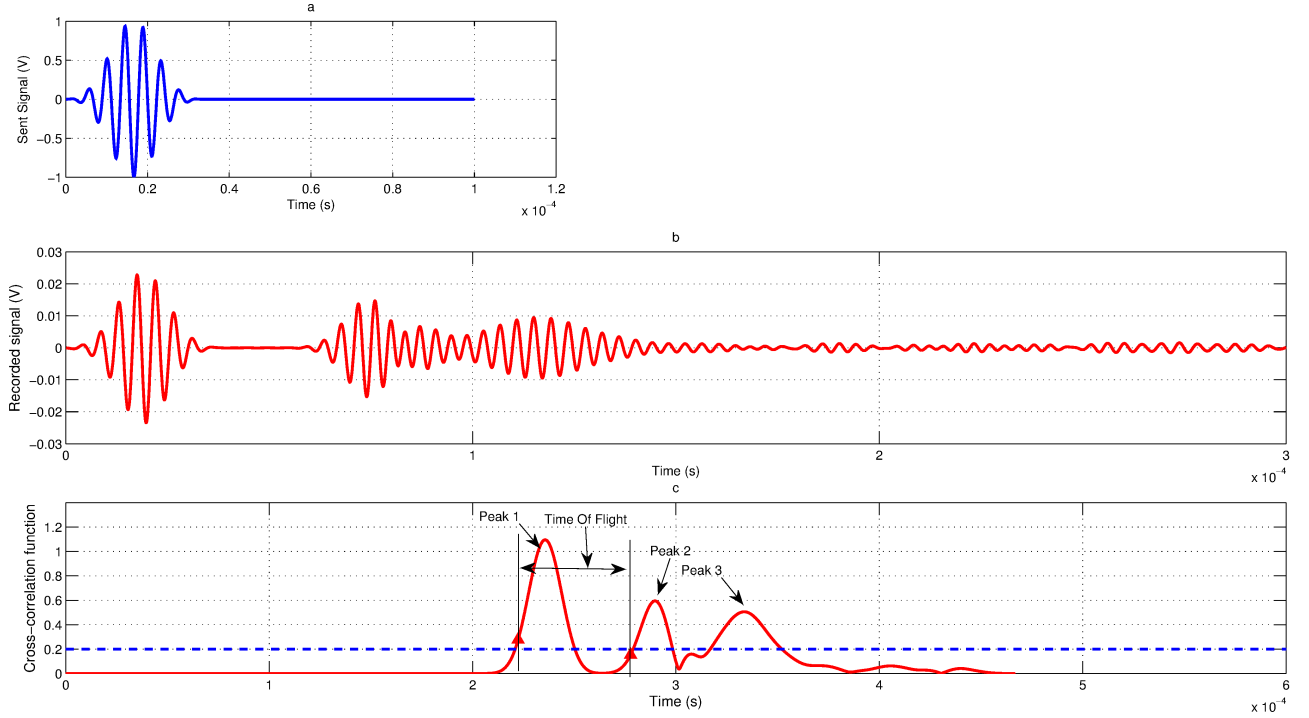


Fig. 3. (a) Input signal at 225 kHz. (b) Transmitted signal recorded by the first channel. (c) Cross-correlation of the input signal and the received signal. The dashed line represents the threshold used in the processing discussed in Section II-B.

There are a number of different ways to determine sound speed from a pulse transmitted between a source and receiver. Broadband measurements based on the phase spectrum difference between transmissions in sand and water are often used in laboratory (see e.g. [13]) for their ability to compute phase speed over a large frequency band with a single signal. This technique requires the transmission of long frequency-modulated signals and in the case of the INSEA, reflections from the stakes as well as the sediment interface would interfere with the direct path, corrupting the phase of the received signal. Consequently, we chose to send relatively short, harmonic pulses and instead estimate the phase speed at the center frequency of each pulse.

Buckingham and Richardson [4] note that the signal transmitted into the sediment is going to be distorted relative to input waveform due to both the band-limited source and the mass-loading of the transducers by the sediment. As a consequence, they argue that the errors due this distortion can be avoided by using the cross-correlation between the two received signals to determine time-

of-flight instead of the cross-correlation between the transmitted and the received signals. Since both receivers are measuring the same transmitted signal, the distortions should be nearly identical and hence reduce the errors in the measurement. This procedure, however, supposes that there is a sufficient distance between the two receivers to reduce the uncertainty in the time-of-flight. In the case of the ISSAMS, this distance is 0.53 m. In order for the INSEA to be a diver-portable instrument, the distance between the sources and receivers needs to be much less than those for the ISSAMS. Considering that we must respect a minimum distance between the emitter and the receiver, typically 10 cm, this leads to a small separation between the two receivers. The resulting uncertainty is further exacerbated by reflections from the sediment interface and from the stakes. This makes it difficult to have an automatic procedure for computing the sound speed from the cross-correlation between the received signals. Therefore, we preferred to work with the correlation between emitted and received signals, a method that is regularly used within the geotechnical community (see e.g. [14]), or for *in-situ* acoustic measurements [15]. With this approach, the sound speed is then computed as

$$c(f) = \frac{d_{sr}}{t_{sr}}, \quad (1)$$

where d_{er} is the distance between the sources and the receiver, t_{er} is the time-of-flight determined from the cross-correlation of the transmitted pulse and the received pulse, and f is the frequency.

The input waveforms are a series of tonal pulses, each possessing between 5 and 8 cycles, modulated by a Blackman-Harris envelope, with central frequencies from 70 kHz to 375 kHz, in 25 kHz increments (Fig. 3a). The modulation is used to reduce the distortion due to the source bandwidth, while the number of cycles is adjusted to ensure a balance between the duration of the signal and their bandwidth. For the TREX13 measurements, 17 signals were transmitted each time the system was inserted into the sediment. Note that the choice of transmitted signals is arbitrary and the user can define waveforms of different shapes or frequencies.

The signals with frequencies lower than 125 kHz are sent to source T1 and the other ones are sent to source T2. They are amplified with 40 dB gain. After propagation in the sediment, the signals are received by the two receivers, amplified with 15 dB gain, and sampled at 10 MHz. This processing is performed onboard the INSEA using the same electronic card.

The cross-talk phenomenon inside the INSEA is such that both the transmitted and received signals are recorded on each channel. The example displayed in figure 3b shows that the received

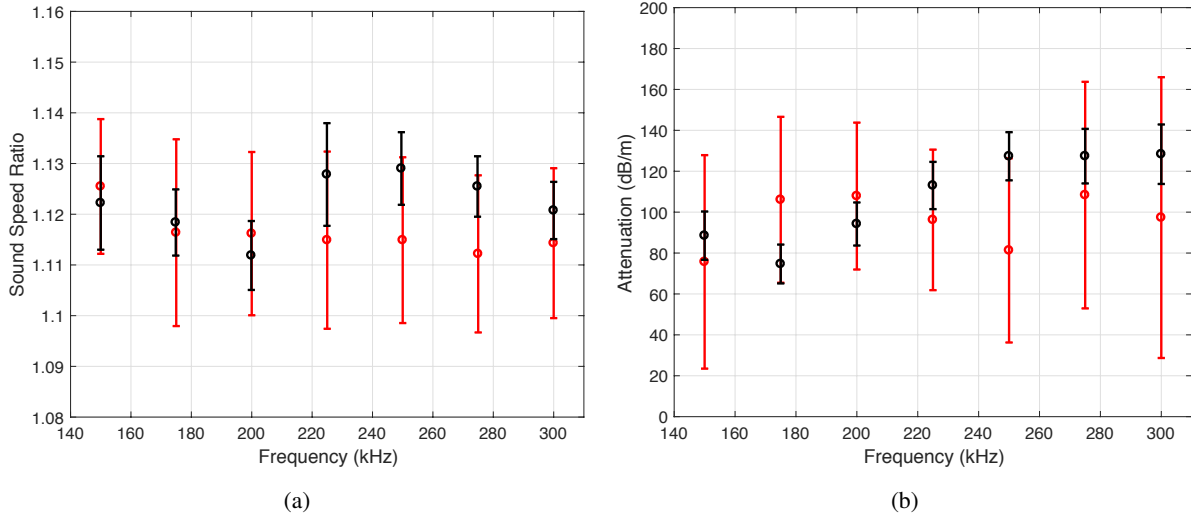


Fig. 4. (a) Comparison of the sound speed ratio results for Site M1 using the processing in Section II-B (black) and the phase delay timing technique developed in [4] (red). (b) Comparison of the attenuation results for Site M1 using the processing in Section II-C (black) and the inter-receiver attenuation developed in [4].

signal is composed of direct and reflected acoustic paths, leading to a longer signal. The cross-correlation of this signals with the input signal is computed and the peaks in the correlation which exceed some empirical threshold are identified. The time-of-flight is then found from the difference between the times at which the correlation function reaches 25% of the leading edge of the two first peaks (Fig. 3.c). This procedure is chosen to reduce the influence of the degradation of the signal tail on the cross-correlation function.

To determine precisely the distance, d_{sr} , between the acoustic centers of the sources and receivers, the INSEA is also triggered by the diver to collect data when the stakes are in the water near the sediment. The procedure discussed above is then used to determine the time-of-flight in water, t_w . Using the temperature and salinity measured at the same location by a CTD, the sound speed c_w is found using the Chen and Millero algorithm [16] and this is used to determine the distances between sources and receivers, $d_{sr} = c_w \times t_w$. For the INSEA, this distance has been found to vary with frequency and may be due to a frequency-dependent phase response inherent in the system. While the source of this response is unknown, the consequence of this fluctuation on the INSEA performances is discussed in section II-D.

In order to verify that this technique produces results comparable to other processing approaches, the data from Site M1 discussed in Section III was also processed using the inter-

receiver phase delay timing described in [4] (Fig. 4a). The uncertainties shown are due solely to statistical variations and not intrinsic errors in the system. This uncertainty is significantly larger for the inter-receiver processing since the small distance between the receivers (3.5 cm) leads to large relative errors in the phase calculation. The distance between the transmitter and the receiver is longer (10 cm), hence errors in the correlation calculation do not produce as large an uncertainty. There is, however, more variation in the mean sound speed as a function of frequency which may be due to the difference in the frequency-dependent responses of the transducers when they are in water and in the sediment. This variation falls within the error bars of the phase delay technique indicating that these two processing methods produce comparable results for the INSEA.

C. Attenuation measurements

The absorption coefficient, α (in Neper/m), is obtained from the amplitudes of the propagated signals in the water A_w and in the sediment A_s . Due to the scattering and multipath effects, the spectra of the received signals are difficult to exploit and, therefore, we used the amplitudes of the received temporal signals. The received amplitudes are $A_w = A_0/d_{er}$ and $A_s = (A_0/d_{er}) e^{-\alpha d_{er}}$ where A_0 is the amplitude of the transmitted signal. The ratio of these amplitudes yields

$$e^{-\alpha d_{er}} = \frac{A_s}{A_w}. \quad (2)$$

In this equation, absorption in water is neglected since, according to the Francois and Garrison model [17], absorption in water in usual conditions is 0.05 dB for 40 cm at 350 kHz. The sediment attenuation is then converted into more conventional units, leading to β in dB/λ or κ in dB/m,

$$\beta = \frac{8.686 \times c \times \alpha}{f} \quad \text{and} \quad \kappa = 8.686\alpha, \quad (3)$$

where c is the sediment sound speed. With this simple procedure, β can be estimated even with the ignorance of the emission and acquisition chain. Nevertheless, it is assumed that amplitude A_0 is the same in the water and in the sediment. This assumption is discussed in section II-D.

As was done for the sound speed processing, the results of the attenuation processing technique described here were also compared with the inter-receiver attenuation technique developed in [4] (Fig. 4b). Again the inter-receiver approach exhibits large uncertainties due to the short distance between the probes which increases the effects of errors in the Fourier amplitude calculations.

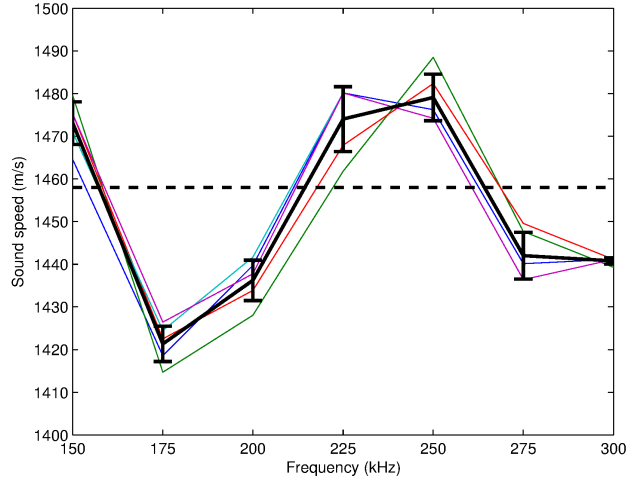


Fig. 5. Sound speed measured in Shell™ rimula 15W4 oil at 5 different points. Solid black curve is the mean and the 95 % confident interval of the measurements. Dashed horizontal line is the theoretical sound speed.

There are also significant variations in the mean attenuation levels comparable to, if not larger, than the single receiver processing approach. The single receiver approach results again fall within the uncertainties of the inter-receiver approach indicating that the two approaches produce comparable results for this device.

D. Uncertainties, calibration, and verification

Intrinsic errors in the INSEA measurements are due to numerous factors that might affect the estimation of time-of-flight, distances, and amplitudes of the signals: sampling frequency, temperature and salinity estimation, pH of water, resolution of the cross-correlation function, etc.

To examine the intrinsic error in the sound speed, we performed 5 measurements in a reference liquid, the Shell™ rimula 15W40 oil, at different locations in a small tank in order to estimate these uncertainties and the repeatability of the INSEA. The strongest difference in sound speed estimation is around 15 m/s (Fig. 5) which is similar to other types of systems (see e.g. [18]).

The attenuation coefficient of this reference liquid is too small to be used to estimate the uncertainty in the INSEA attenuation processing and, to the knowledge of the authors, there is no standard reference medium for compressional wave attenuation. Again, we expect that the

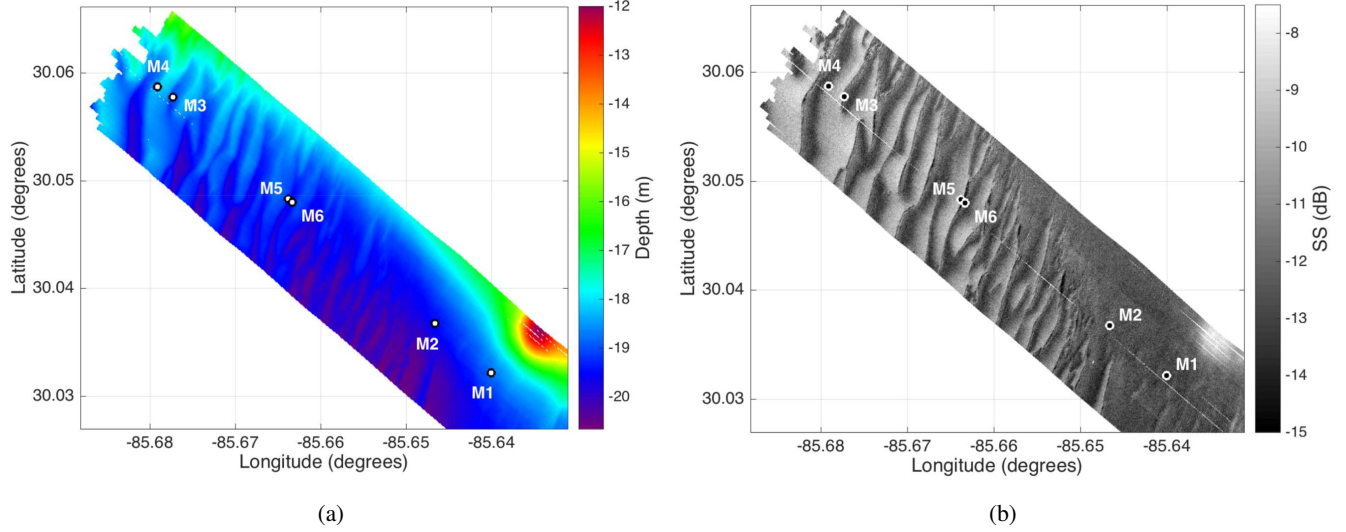


Fig. 6. INSEA deployment locations along the TREX13 main reverberation track in relation to the (a) bathymetry and (b) backscatter measured by DeMoustier and Kraft during the multibeam echosounder survey. The units of the color scale in (a) are meters relative to sea level. The units of the color scale in (b) are dB.

change in transducer response affects the emitted amplitude A_0 . Because it is quite difficult to compensate for these mechanisms, we calibrate the INSEA attenuation measurement *a posteriori*. The absorption coefficient is measured with the INSEA in a reference medium made of 650- μ m diameter glass beads. In such medium, assuming a porosity of 38 % and a 10-cm burial depth, the Grain Shearing model [19] predicts a mean value of 0.45 dB/ λ at the considered frequency range for the absorption coefficient. The corrective term is therefore given by

$$\beta_{cor} = \beta_{INSEA} - 0.45. \quad (4)$$

β_{cor} is then applied to all measurements. This was done, for example, for the results in Fig. 4b.

III. ACOUSTIC AND GEOLOGICAL DATA

A. Experiment site

The INSEA measurements took place at the site of TREX13, a field experiment jointly sponsored by the Office of Naval Research (ONR) and the Strategic Environmental Research and Development Program (SERDP). The experiment consisted of two major components: a synthetic aperture sonar (SAS) experiment and a mid-frequency reverberation experiment. The

TABLE I

MEASUREMENT SITES WHERE DATA WAS COLLECTED ON THE 3RD OF JUNE, 2013 WITH THEIR CHARACTERISTICS.

Site	Coordinates	Depth (m)	Temp. (°C)	Insertions at site
M1	30°1.902' N 85°38.400' W	19.4	25.4	16
M2	30°2.179' N 85°38.789' W	20.0	25.5	14
M4	30°3.515' N 85°40.719' W	20.0	25.4	15
M5	30°2.883' N 85°39.811' W	19.8	25.5	16
M6	30°2.865' N 85°39.784' W	19.5	25.5	13

SAS experiment utilized a rail-mounted sonar system to study target scattering from 1–100 kHz for mine-countermeasures and unexploded ordinance detection. The rail system was deployed from the R/V Hugh R. Sharp, which was stationed in a four-point moor in 19 m of water. While the ship was in the mooring, a horizontal line array also was mounted on the seafloor and this system, in conjunction with a bottom-mounted source, measured reverberation at 1–10 kHz from a 7-km-long track running away from the R/V Sharp to the southwest approximately along an isobath. A multibeam survey was conducted along this track by Drs. Chris de Moustier and Barbara Kraft using a Teledyne-RESON Seabat 7125 multibeam echosounder (MBES) to measure the bathymetry and grazing-angle-normalized, 400 kHz acoustic backscatter from the seafloor. Portions of this survey are shown in Fig. 6. The R/V Sharp was moored just to the northwest of the point labeled M4.

In addition to the acoustic measurements collected during the experiment, extensive environmental characterization was also performed to support data/model comparisons for both experimental efforts. The site consisted of a series of sand ridges running roughly perpendicular to the reverberation track. These ridges have a 100–200 m wavelength with an amplitude of roughly 1 m. Coring and grab samples showed that the shell content within each ridge increased from 1% of the total sediment weight on the northwest face to as high as 11% near the base of the southwest face. This is the likely cause of the increase in the scattering strength across each ridge in Fig. 6b. Between the ridges, at the base of each southeast face, were narrow regions that had a thin surface layer of mud over the sand and appear as the lowest scattering strengths in Fig. 6b. With this variation in the sediment properties across the experiment site, the sediment

TABLE II
GEOLOGICAL PARAMETERS OF THE SEDIMENTS COLLECTED AT THE MEASUREMENT SITES.

	M1	M2	M4	M5	M6
Classification	Fine Sand	Fine Sand	Sand	Sand	Fine Sand
Mean Grain Size (mm)	0.237	0.249	0.642	0.722	0.302
Mean Grain Size (ϕ)	2.075	2.009	0.639	0.471	1.729
Sorting	0.775	1.079	1.165	1.242	0.716
Skewness	-0.074	-0.167	-0.148	-0.197	-0.028
Kurtosis	1.218	1.143	1.560	1.777	1.087
CaCo ₃ %	1	4	22	18	1
Porosity	0.44	0.45	0.48	0.46	0.43
Bulk Density	1.924	1.913	1.863	1.907	1.946

sound speed and attenuation were expected to vary as well. To capture this variation, both the SAMS and the INSEA were deployed at a number of locations along the track. These locations were chosen based partially on the 400-kHz backscatter and on the deployment locations of other acoustic measurements made during the experiment. The SAMS was designed to collect data from 1–10 kHz using sources mounted on a frame positioned immediately above the sediment interface and a receiver that was inserted up to 3 m into the sediment using a water jet. Details of these measurements are given in [20]. Although these measurements provide sound speed and attenuation in the frequency band of the reverberation measurements, the INSEA was deployed to cover a portion of the frequency range of the SAS measurements and, combined with the SAMS data, provide a broad band of frequencies needed to test theories of sediment propagation.

B. Acoustic data acquired with INSEA

The INSEA was deployed from a dive boat at 5 locations along the main TREX13 reverberation track, as indicated in Fig. 6. The coordinates of these locations are given in Table I. All of the sites along the reverberation track had significant shell content. At each location, the instrument was inserted into the sediment at least 13 times to collect acoustic data. The depth and water temperature were recorded with an autonomous temperature-pressure sensor fixed on the INSEA (Table I). The data from each insertion was used to produce two sound speed and attenuation

curves vs frequency. After analysis of the data, some of these curves were rejected because they exhibited unrealistic behavior (see Section IV).

C. Geological data

At each measurement point, small cofferdams were used to sample the upper 10 cm of the sediment. Samples from the cofferdams were later analyzed by SHOM (Service Hydrographique et Océanographique de la Marine, French Hydrographic and Oceanographic Service) in France. Three types of analyses were performed. First, the grain size distribution is obtained using with 15 different sieves. From this distribution, the cumulative grain size distribution is plotted and various percentiles are obtained from which four statistics are computed according to Folk's prescriptions [21]: mean grain size, sorting, skewness, and kurtosis. Second, the CaCO_3 percentage is measured by the Bernard calcimeter method [22]. And third, the grain density and the porosity are determined by helium pycnometer. From these measurements, the sediment bulk density is estimated. Table II reports the values obtained for these parameters for the 5 sediment samples. Note that the values presented in this table are obtained from a single analysis performed on a single sediment sample.

Photos of the dried sediments at two different scales were taken at the French Naval Academy with a stereo microscope (Figs. 7). M4 and M5 samples have a lot of shell hash. This is supported by their CaCO_3 percentage. The three remaining sites (M1, M2, and M6) contain less shell pieces, which nevertheless may have some impact on the acoustic measurements.

In order to analyzed the shell content in greater detail, sediment collected from additional cofferdams at each site was also sieved on site to extract material greater than 2.0 mm in diameter. The remaining material was primarily shell and shell hash and these samples were later sieved to determine the shell size distribution between 2.0 mm and 9.5 mm (Fig. 8). The shell size distributions for Sites M1 and M6 were similar to that measured during SAX04 [23], [24]. Across the site, the shell content was found to vary by roughly an order of magnitude, with the largest content occurring on the eastern slopes of the sand ridges. Assuming a grain density of 2.7 g/cm^3 , the shells above 2 mm in diameter account for 0.3% of the sediment volume at site M1 and 6.0% of the sediment volume at site M5. In examining the role of shell pieces in volume scattering, Lyons concluded that single scattering theories should be adequate if the volume concentration is 1% or less [25]. Both sites M4 and M5 exceed this threshold, indicating

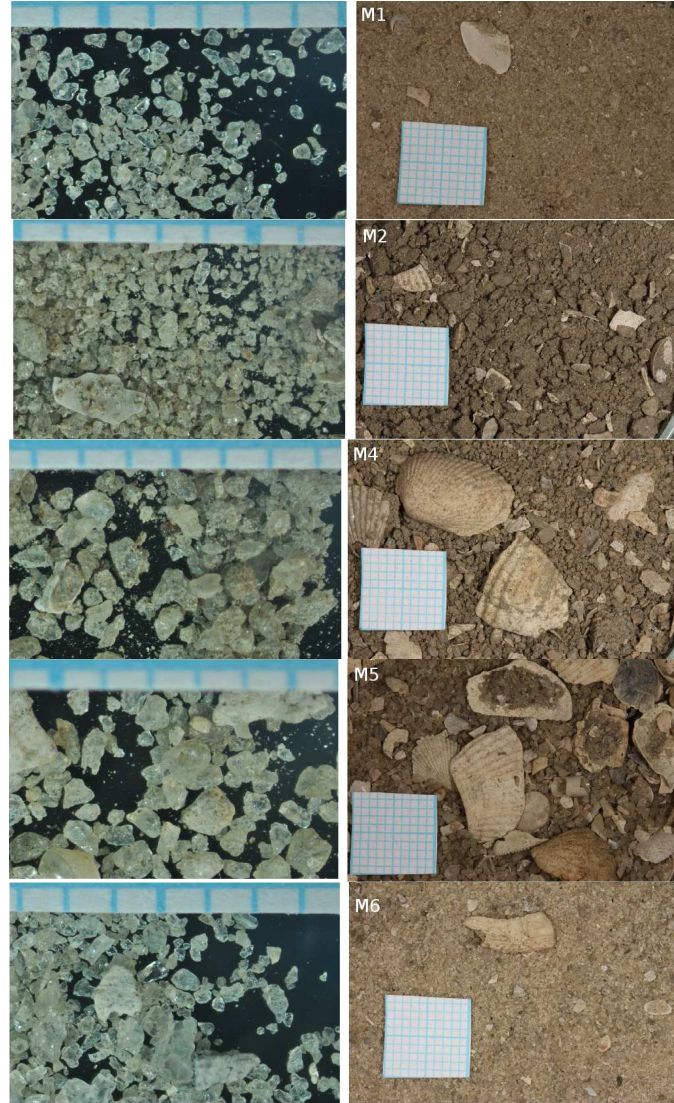


Fig. 7. Sediment from Sites M1 (1st row), M2 (2nd row), M4 (3rd row), M5 (5th row), and M6 (6th row). On all photos the small blue squares are 1 mm \times 1 mm.

that for these sites multiple scattering effects become important and as a result, the shells should have a significant effect on sound propagation within the sediment.

IV. ANALYSIS OF THE RESULTS

Fig. 9 shows the sound speed ratio (SSR) and attenuation in dB/m for the 5 sites. As mentioned in section II-A, only data within the octave 150 kHz - 300 kHz was analyzed. For each site, we compute the mean and the 95% confident interval using data from multiple insertions at each

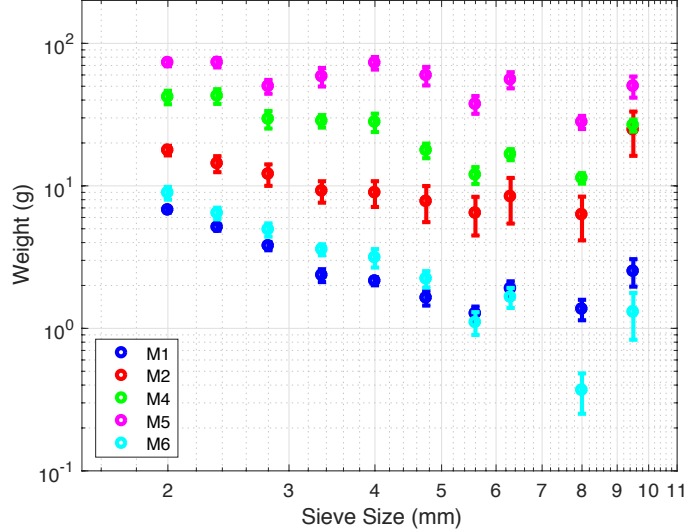


Fig. 8. Distribution of shell weights as a function of sieve size. While this type of data is typically presented as a histogram, it is shown here as a scatter plot on a log-log scale to facilitate comparisons between data collected at different sites and to emphasize the power-law behavior exhibited by several of the sites.

site which are shown as the colored lines in the figure. Data from each insertion were compared to the mean at that site and those data which showed erratic frequency dependence or very high or low values were rejected. This rejected data is not displayed in Fig. 9 nor was it used to calculate the displayed mean values and associated error bars.

For the measured sound speed ratios, sites M1, M2, and M6 show little-to-no dispersion, while sites M4 and M5 show significant negative dispersion. These latter sites both had very high shell content and the negative dispersion is likely a consequence of the scattering effects mentioned in the previous section. A similar negative dispersion has been observed in fluid-saturated glass beads when the acoustic wavelength in the fluid is on the order of the grain diameter [26]. That dispersion is well-described by multiple scattering models [27], [28], and although the volume fractions in those cases are very high ($\sim 60\%$), these models also predict negative dispersion for lower volume fractions such as those measured at sites M4 and M5.

The frequency dependence of the measured attenuation also appears to be related to the shell content. For ocean sediments, the high-frequency attenuation often goes as f^n where n is the power-law exponent. For granular sediments, such as the sand sediments at SAX99 and SAX04 or the saturated glass beads used in laboratory measurements, $n \approx 1$ as long as $ka \ll 1$ where

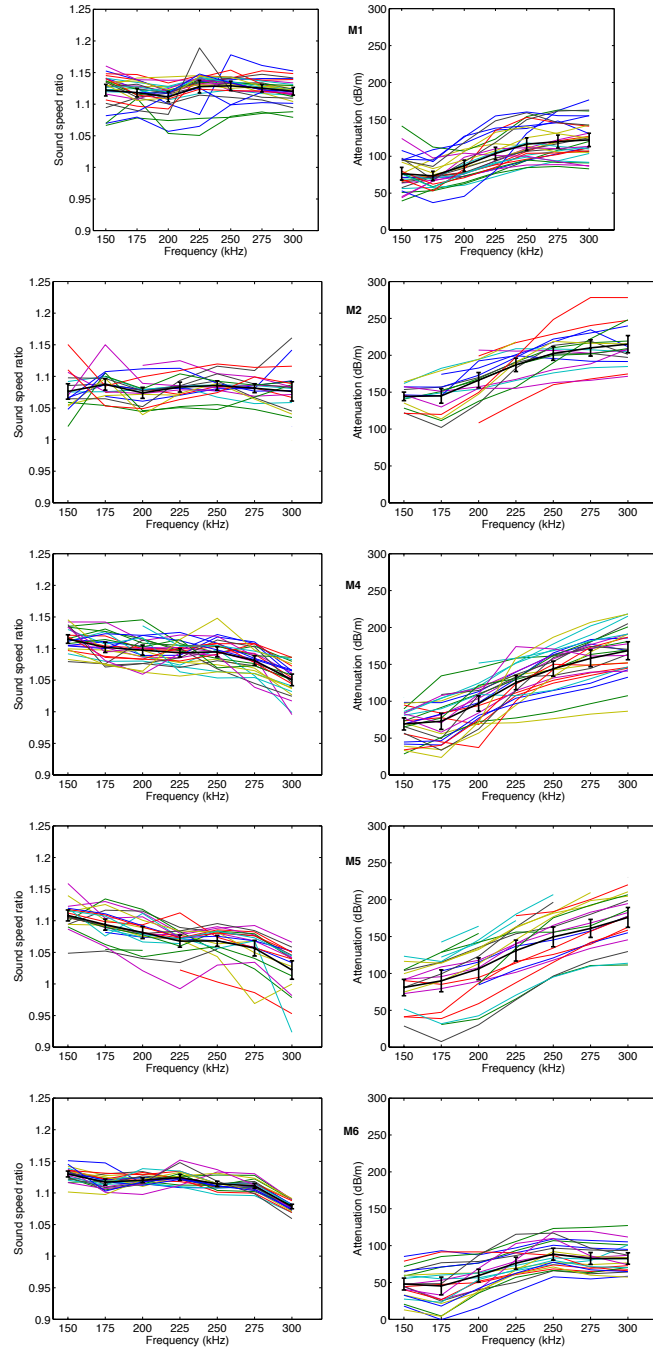


Fig. 9. Sound speed ratios (left column) and attenuations (right column) obtained from sites M1 (1st row), M2 (2nd row), M4 (3rd row), M5 (5th row), and M6 (6th row). The color lines are the individual measurements of the sound speed and attenuation found using different combinations of sources and receivers on the INSEA and for different insertions at each site. The black lines are the mean values and the 95% confidence limits obtained from the individual measurements.

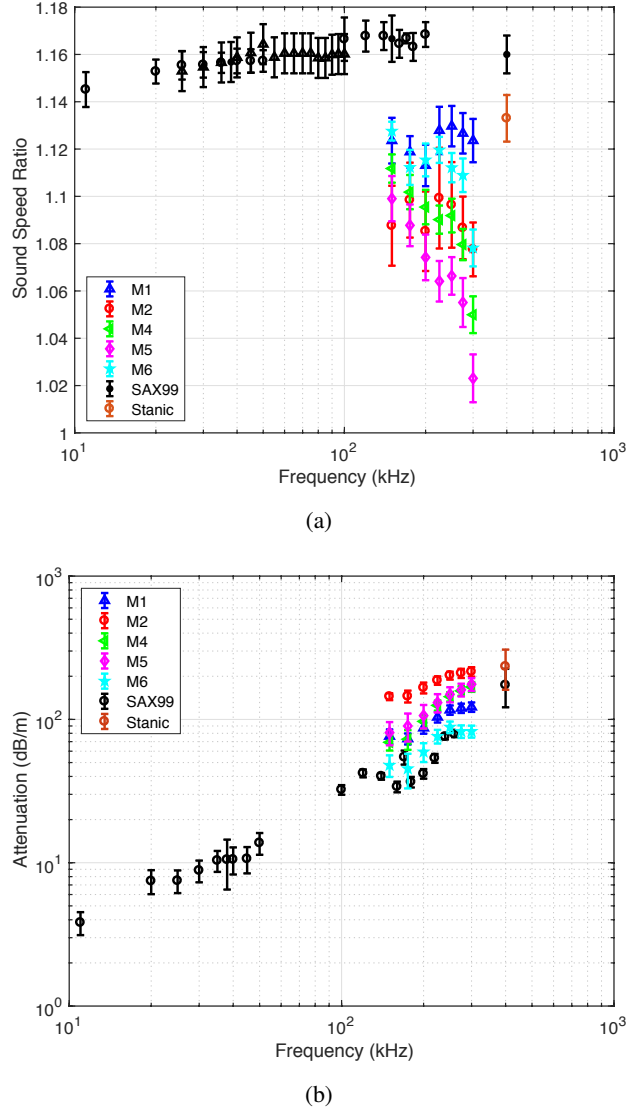


Fig. 10. Comparisons of (a) the sound speed ratios and (b) attenuations measured during TREX13 to those measured during SAX99 off Ft. Walton Beach, FL and those measured by Stanic of Panama City Beach, FL.

k is the wavenumber in the fluid and a is the grain diameter. For the TREX13 sediments, the attenuations measured at the sites with lower shell content follow a power-law frequency with $n \leq 1$ (Table III). At sites M4 and M5, the frequency dependence is slightly larger, with $n = 1.40 \pm 0.19$ for site M4 and $n = 1.19 \pm 0.13$ for site M5. Given the dispersion measured at these two sites, it seems likely that the increase in the frequency dependence of the attenuation is due to scattering from the shell pieces.

While the results from sites M1 and M6 are consistent with propagation within a sand sediment

in the absence of shells, the sound speed ratio and attenuation measured at site M2 is notably different. The sound speed ratio is significantly lower than sites M1 and M6 ($\Delta\text{SSR} \approx 0.04$) and the attenuation is much higher than any of the other sites. Although it has a slightly higher shell content than the other two sites, it is not nearly at the levels of sites M4 and M5. Also there is nothing in the geological parameters in Table II to indicate that the sediment should behave any different. One possible explanation may be that the sediment at site M2 was a mix of mud and sand or contained pockets of mud and this mud was lost during the sampling procedure or was not captured in the geological analysis. This would be consistent with observations of mud at other locations within the TREX13 experiment site and the multibeam backscatter at the site, but without actual measurements of the mud content, this remains speculation.

The results from TREX13 are compared in Fig. 10 to published results acquired at nearby sites. The SAX99 experiment took place off of Ft. Walton Beach, FL, roughly 90 miles to the west of the TREX13 site at roughly the same water depth [29]. For the TREX13 sites with low shell content, the lack of dispersion is consistent with that observed during SAX99 but the values are significantly lower ($\Delta\text{SSR} \approx 0.04$). This corresponds to a sound speed difference of roughly 60 m/s. The TREX13 sound speed ratios are consistent with the 500 kHz sound speed measurement made by Stanic et. al. in roughly the same area as TREX13 [30]. At lower frequencies (1–10 kHz), Yang et. al. measured sound speeds at the TREX13 site that were lower than those measured for SAX99 by a similar amount. These comparisons support the results of the INSEA sound speed measurements and indicate a large scale spatial variation in the sediment properties along this stretch of the West Florida sand sheet.

For those sites at TREX13 which have low shell content, the attenuation levels are roughly the same as those measured in SAX99 despite the differences in the sound speed ratios. This is

TABLE III

POWER-LAW EXPONENT, n , AND ITS STANDARD DEVIATION, σ_n , FOR THE FREQUENCY DEPENDENCE OF THE ATTENUATION MEASURED AT EACH SITE. THESE WERE DETERMINED FROM A LINEAR REGRESSION OF $\log(\alpha)$ WITH RESPECT TO $\log(f)$.

	M1	M2	M4	M5	M6
n	0.84	0.66	1.40	1.19	0.93
σ_n	0.13	0.06	0.09	0.07	0.15

not surprising since at high-frequencies, the parameters that most impact the sound speed ratio for poroelastic models (grain modulus, porosity, and grain density) have very little effect on the attenuation levels (See Figures 1 and 2 in [29]). The attenuation levels do increase, however, with the increasing in shell content, consistent with the increase in dispersion.

V. CONCLUSION

The INSEA prototype, a small, diver-deployed acoustic array, was used to make in-situ sediment sound speed and attenuation measurements at locations along the main reverberation track at TREX13. The automated processing technique which utilizes the cross-correlation between the input signal and the received signals is comparable in accuracy to phase delay techniques and allows for rapid determination of geoacoustic properties of the sediment. The measurements reported here indicate that shells play an important role in high-frequency dispersion and attenuation in the TREX13 sediment. This is consistent with models of scattering loss within the sediment and may have important implications for high-frequency scattering from the sediment. In the absence of shells, the sound speed was lower than that measured in other sand sediments but is consistent with previous measurements made in the same area of the Gulf of Mexico. The measured attenuation is also consistent with that measured in other sand sediments, however one site shows anomalously low sound speed and high attenuation. This may reflect the presence of mud at the site which was not captured by the environmental characterization.

ACKNOWLEDGMENT

The authors would like to thank the funding agencies of this project: ONR, SERDP, ONRG, DGA. They thank also the crew from the dive boat and people from APL-UW for the in-situ measurements. Finally, they want to thank Patrick Guyomard (SHOM) for geological measurements and Joseph Poupin (IRENav) for sediment pictures.

REFERENCES

- [1] N. Chotiros and M. J. Isakson, "Shear wave attenuation and micro-fluidics in water-saturated sand and glass beads," *J. Acoust. Soc. Am.*, vol. 135, no. 6, pp. 3264–3279, 2014.
- [2] M. Buckingham, "On pore-fluid viscosity and the wave properties of saturated granular materials including marine sediments," *J. Acoust. Soc. Am.*, vol. 122, no. 3, pp. 1486–1501, 2007.

- [3] J. Goff, B. Kraft, L. Mayer, S. Schock, C. Sommerfield, H. Olson, S. Gulick, and S. Nordfjord, "Seabed characterization on the new jersey middle and outer shelf: correlatability and spatial variability of seafloor sediment properties," *Marine Geology*, vol. 209, pp. 147–172, 2004.
- [4] M. J. Buckingham and M. D. Richardson, "On tone-burst measurements of sound speed and attenuation in sandy marine sediments," *IEEE Journal of Oceanic Engineering*, vol. 27, no. 3, pp. 429–453, 2002.
- [5] J. Yang, D. Tang, and K. L. Williams, "Direct measurement of sediment sound speed in shallow water '06," *J. Acous. Soc. Am.*, vol. 124, no. 3, pp. EL116–EL121, 2008.
- [6] Rtsys website. [Online]. Available: <http://www.rtsys.eu/en>
- [7] X. Demoulin, L. Guillon, R. Bourdon, L. Dufrechou, P. Guyomard, and T. Garlan, "A portative celerimeter for measurement and analysis of compressional speed and attenuation in marine sediments: description and first results," in *Acoustics 2012 Conference*, Nantes, France, 2012, pp. 63–68.
- [8] ——, "A new portable velocimeter for sound speed measurement in sandy seafloors," in *11th European Conference on Underwater Acoustics*, C. Capus, Ed., Edinburgh, UK, 2012, pp. 60–67.
- [9] X. Demoulin, L. Guillon, T. Garlan, and P. Guyomard, "Sound speed and attenuation measurements in sandy sediments: comparisons between tank measurements, in-situ measurements, and theoretical predictions," in *1st Int. Conf. and Exhibition on Underwater Acoustics*, J. Papadakis and L. Bjorno, Eds., Corfou Island, Greece, 2013, pp. 927–934.
- [10] D. Jackson and M. Richardson, *High-frequency seafloor acoustics*. Springer, 2007.
- [11] K. Lee, "Frequency dependencies of phase velocity and attenuation coefficient in a water-saturated sandy sediment from 0.3 MHz to 1 MHz," *J. Acous. Soc. Am.*, vol. 121, pp. 2553–2558, 2007.
- [12] B. Hefner and K. Williams, "Sound speed and attenuation measurements in unconsolidated glass-bead sediments saturated with viscous pore fluids," *J. Acoust. Soc. Am.*, vol. 120, pp. 2538–2549, 2006.
- [13] P. He, "Direct measurement of ultrasonic dispersion using a broadband transmission technique," *Ultrasonics*, vol. 37, pp. 67–70, 1999.
- [14] S. Yamashita, T. Fujiwara, T. Kawaguchi, T. Mikami, Y. Nakata, and S. Shibuya, "International parallel test on the measurement of gmax using bender elements organized by tc-29," *ISSMGE TC-29 Report*, pp. 1–76, 2007.
- [15] K. M. Lee, M. S. Ballard, A. R. McNeese, T. G. Muir, P. S. Wilson, R. D. Costley, and K. K. Hathaway, "In situ measurements of sediment acoustic properties in currituck sound and comparison to models," *J. Acous. Soc. Am.*, vol. 140, no. 5, pp. 3593–3606, 2016.
- [16] C. Chen and F. Millero, "Speed of sound in seawater at high pressures," *J. Acous. Soc. Am.*, vol. 62, no. 5, pp. 1129–1135, 1977.
- [17] R. Francois and G. Garrison, "Sound absorption based on ocean measurements. part II: Boric acid contribution and equation for total absorption," *The Journal of the Acoustical Society of America*, vol. 72, no. 6, pp. 1879–1890, 1982.
- [18] G. B. N. Robb, A. I. Best, J. K. Dix, J. M. Bull, T. G. Leighton, and P. R. White, "The frequency dependence of compressional wave velocity and attenuation coefficient of intertidal marine sediments," *J. Acoust. Soc. Am.*, vol. 120, no. 5, pp. 2526–2537, 2006.
- [19] M. Buckingham, "Compressional and shear wave properties of marine sediments: comparisons between theory and data," *J. Acoust. Soc. Am.*, vol. 117, no. 1, pp. 137–152, 2005.
- [20] J. Yang, "Mid-frequency sound speed and attenuation measurements at TREX13," *IEEE Journal of Oceanic Engineering*, 2016, submitted.

- [21] R. L. Folk and C. W. Ward, "Brazos river bar: a study in the significance of grain size parameters," *J. Sediment. Petrol.*, vol. 27, no. 1, pp. 3–26, 1957.
- [22] J. Hulseman, "An inventory of marine carbonate materials," *J. Sediment. Petrol.*, vol. 36, no. 2, pp. 622–625, 1966.
- [23] A. N. Ivakin, "High frequency scattering from sandy sediments: roughness vs discrete inclusions," in *Boundary Influences in High Frequency Shallow Water Acoustics*, N. G. Pace and P. Blondel, Eds. University of Bath, UK, 2005, pp. 185–192.
- [24] ——, "Discrete scattering in stratified marine sediments: A modeling approach and application to a shelly sand-mud environment," in *Tenth European Conference on Underwater Acoustics ECUA*, 2010, pp. 1432–1439.
- [25] A. Lyons, "The Potential Impact of Shell Fragment Distributions on High-Frequency Seafloor Backscatter," *IEEE J. Ocean. Eng.*, vol. 30, no. 4, pp. 843–851, Oct. 2005.
- [26] K. Lee, E. Park, and W. Seong, "High frequency measurements of sound speed and attenuation in water-saturated glass-beads of varying size," *J. Acoust. Soc. Am.*, vol. 126, no. 1, pp. EL28–EL33, 2009.
- [27] K. Lee, H. Yang, and W. Seong, "Acoustic Rayleigh scattering in water-saturated granular medium with quasicrystalline approximation," *J. Acoust. Soc. Am.*, vol. 137, no. 5, pp. EL367–EL373, May 2015.
- [28] L. Tsang, "Multiple scattering of acoustic waves by random distribution of discrete spherical scatterers with the quasicrystalline and Percus–Yevick approximation," *J. Acoust. Soc. Am.*, vol. 71, no. 3, p. 552, 1982.
- [29] K. L. Williams, D. R. Jackson, E. I. Thorsos, D. Tang, and S. G. Schock, "Comparison of sound speed and attenuation measured in a sandy sediment to predictions based on the Biot theory of porous media," *IEEE J. Ocean. Eng.*, vol. 27, no. 3, pp. 413–428, 2002.
- [30] S. Stanic, K. B. Briggs, P. Fleischer, R. Ray, and W. Sawyer, "Shallow-Water High-Frequency Bottom Scattering Off Panama-City, Florida," *J. Acoust. Soc. Am.*, vol. 83, no. 6, pp. 2134–2144, Jun. 1988.

OVERVIEW OF THE REVERBERATION COMPONENT OF TREX13

Brian T. Hefner^a, Dajun Tang^a

^aApplied Physics Laboratory, University of Washington, 1013 NE 40th Street, Seattle, WA 98105-6698, USA

Brian T. Hefner, Applied Physics Laboratory, University of Washington, 1013 NE 40th Street, Seattle, WA 98105-6698, USA, FAX: (206) 543-6785, hefner@apl.washington.edu

Abstract: *In the spring of 2013, a shallow water reverberation experiment was conducted to measure contemporaneous acoustic and sufficient environmental data so detailed model/data comparisons could be achieved and important environmental factors could be identified for different applications. The Target and Reverberation Experiment (TREX13) was sponsored by the US Office of Naval Research (ONR) and the Strategic Environmental Research and Development Program (SERDP). It was conducted from April to June of 2013 off the coast of Panama City Beach, Florida, in collaboration with multiple institutions and involving three research vessels: The R/V Sharp, R/V Walton Smith, and the Canadian Force Auxiliary Vessel (CFAV) Quest. From a SONAR viewpoint, reverberation consists of two-way propagation and a single backscatter. Therefore, reverberation, transmission loss, and bottom backscatter were repeatedly measured over a time period of several weeks in the frequency band of 2-10 kHz, along with extensive environmental measurements. To reduce the area over which environmental measurements were needed, the reverberation was measured using a horizontal line array mounted on the seafloor in 19 m of water. The reverberation, transmission loss, and bottom backscatter were measured along a single beam of the array out to a distance of 7 km. Discussed will be planning and execution of the field experiments, strategies and steps for data analysis, and modeling efforts.*

Keywords: TREX13, Reverberation, Transmission Loss

1. INTRODUCTION

The detection of underwater targets in shallow water is in many cases reverberation limited. This has led to a plethora of reverberation models that have increased in complexity over time as computational capabilities have improved. Despite the availability of these modeling tools, the relative importance of the various environmental factors that affect reverberation is not well understood. This difficulty stems from the complexity of the reverberation problem, apparent in the sonar equation,

$$RL = SL - 2 \times TL + SS,$$

where RL is the reverberation level, SL is the source level, TL is the transmission level, and SS is the integrated scattering strength. For example, in this single scattering approximation, while the backscatter from the sea surface roughness may be weak compared to the seafloor roughness, the surface's affect on transmission loss can still be important for the overall reverberation level [1].

This lack of understanding continues despite a number of careful shallow water reverberation measurements made in different environments and conditions. For naval relevance, these measurements have been made in depths from 50 to 200 m and out to ranges of 100 km [2]. Even using a directional source or receiver, a complete understanding of the environment requires measurements of the surface, water column, bottom, and sub-bottom over a very large area. The scale of this measurement area either means that the environmental characterization is incomplete or that it cannot be performed at the time of the acoustic measurements.

The goal of the Target and Reverberation Experiment (TREX13) was to overcome these difficulties by bringing together a number of acoustic and environmental measurement systems in a very shallow water environment. The TREX13 site, off of Panama City Beach, Florida, is approximately 19 m deep with a seafloor that is predominately sand. While mid-frequency naval sonars do not typically operate in this water depth, a transmitted signal can interact many times with the sea surface and seafloor while traveling only a relatively short range. This is not a *scaled* experiment where decrease in depth would necessitate a proportional increase in frequency. Instead the physics affecting mid-frequency transmission loss and scattering is the same as in an operational environment but is interrogated over a smaller, shallower area that can be characterized relatively quickly with measurements supported by divers.

2. ACOUSTIC MEASUREMENTS

To measure reverberation due to sound propagation over a manageable area, the Four Octave Array (FORA) was used in collaboration with the Applied Research Laboratory at Penn State (ARL-Penn State) [3]. This research array, built to support ONR-funded basic research, has a triplet sub-array cut for 3750 Hz. This portion produces a cardioid beam pattern that allows for port/starboard discrimination and was used during TREX13. The R/V Sharp was placed in a four-point moor at the experiment site and the FORA was deployed on a frame below ship that held the array horizontally 2.1 m above the seafloor.

An ITC-2015 source was mounted on the seafloor behind the FORA and transmitted a suite of pulses from 2-4 kHz.

The reverberation measured by the FORA was beamformed along the two experiment tracks shown in Figure 1: the main track and the “clutter” track. The primary goal was to examine the physics affecting reverberation and hence a majority of the acoustic and environmental measurements took place along the main track. This track started at the location of the R/V Sharp and extended parallel to shore along the isobar running toward the southeast for 7 km.

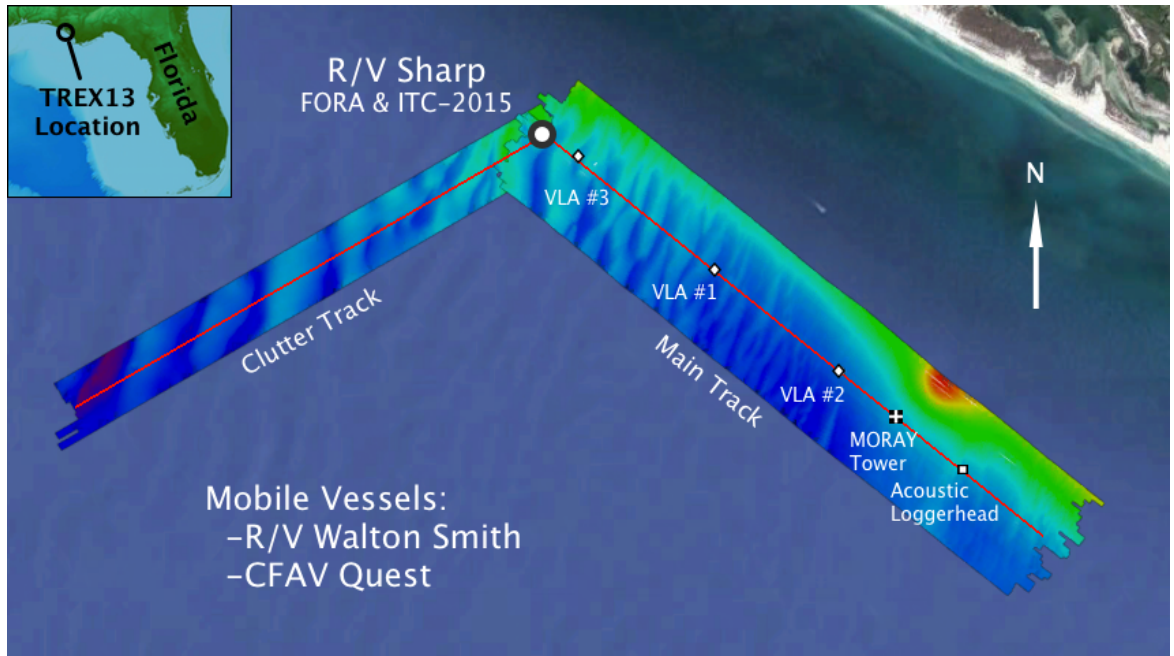


Fig. 1: Map of TREX13 showing the distribution of the long term acoustic sources and receivers. The location of the experiment is shown in the inset. The bathymetric data collected along the two main tracks of the experiment is shown with a linear color scale that goes from 12 m below the sea surface (red) to 21 m (dark blue).

While the FORA was collecting data, two vertical line arrays (VLAs), deployed by the Scripps Marine Physical Lab (MPL) from the R/V Walton Smith, were recording the transmitted signal along the main track at ranges of 2.4 km and 4.2 km. These arrays consisted of 32 elements covering the water column from 5 m to 12.2 m above the seafloor with a spacing of 0.2 m. The VLAs recorded continuously throughout most of the experiment. In addition to measuring the reverberation transmissions, the VLAs were also used in several towed source experiments conducted by MPL to measure bottom loss. Towards the end of the experiment, a third VLA was deployed 500 m from the FORA location to serve as a quasi-monostatic vertical aperture.

Transmission loss data were also collected in conjunction with Defence Research and Development Canada (DRDC) using a horizontal receive array towed by the CFAV Quest. This receive array was part of a larger echo repeater system that provided a target for both the reverberation as well as for continuous active source measurements [4,5]. The towed receiver, VLAs, and autonomous recorders provide TL data along the main track as a

function of both range and time capturing any effects of the seafloor and sub-bottom as well changes to the sea surface roughness due to weather.

In addition to the VLAs, a benthic tower was deployed by APL-UW on the main track, 5 km from the FORA. A 4-element horizontal line array (HLA), a 7-element VLA, a vector sensor, and a DSG-Ocean Acoustic Datalogger were mounted on the tower. This tower was deployed for roughly a week in the middle of the experiment and received transmitted pulses from the ITC-2015 that were also received by the VLAs and the FORA. Several towed source measurements were also made from the R/V Smith that utilized the benthic tower arrays to examine vertical and horizontal coherence [6-8]. The acoustic datalogger recorded continuously while the tower was deployed. A second datalogger was also deployed for the length of the experiment, mounted on the seafloor on the main reverberation track at 6 km.

Scattering strength along the main reverberation track was measured from a drifting dive boat using an ITC-1007 as an omnidirectional source and an ITC-1032 as a receiver. Both transducers were mounted on a bracket and suspended approximately 2 m above the seafloor. The source transmitted CW pulses from 2 to 10 kHz and the receiver recorded the field scattered from a patch of the seafloor with a 17 m radius and covering angles from 9 to 90 degrees.

3. ENVIRONMENTAL CHARACTERIZATION

The use of the FORA limited the environmental characterization needed to test models of reverberation to the area defined by the beam pattern along the main reverberation track that had a nominal horizontal width of 2.4 degrees. To further reduce the characterization burden, the primary area for data/model comparison was limited to a range of 5 km (the location of the benthic tower).

Throughout the deployment of the FORA, two systems were monitoring the sea surface conditions. The first was a wave rider buoy deployed to the south of the R/V Sharp. This measured the directional wave spectrum as a function of time during the experiment. The second system was a camera mounted on the mast of the R/V Sharp. Deployed by Scripps, this system captured images of the sea surface to monitor the formation of white caps, an indicator of bubble plume formation due to plunging waves. In addition to these systems, meteorological data were collected by each ship throughout the experiment. A second wave rider buoy was also deployed at a 5 km range along the main track while the benthic tower was deployed.

Additional oceanographic measurements included daily CTD casts from each of the research vessels and temperature measurements by thermistor chains attached to the Scripps VLAs. These measurements show that the sound speed profile was approximately isovelocity throughout the experiment. Measurements of the current were collected on a second benthic tower deployed to the south of the R/V Sharp location for the duration of the experiment. This system was deployed by NRL-Stennis to measure sediment transport and munitions mobility at the site as part of a separate SERDP-funded effort [9-11]. In addition, a pencil beam sonar on this second benthic tower also measured sea surface wave heights throughout the experiment.

A significant effort was made to characterize the seafloor at the experiment site. A multibeam sonar survey was conducted by the company “10dBx,” both before and after the experiment to provide high-resolution bathymetric data and to monitor any changes that might have occurred at the site during the experiment due to significant weather

events [12]. In addition to bathymetry, the multibeam data were also processed for backscattering strength at 400 kHz. Sediment samples were able to confirm that the high backscatter areas at 400 kHz were composed of sand with significant shell content and the low backscatter areas were predominately mud.

Bottom roughness was measured at a number of locations along the track using two laser line-scanning systems. The first system was deployed by the Applied Research Laboratory, University of Texas (ARL:UT) and is mounted on a remotely operated vehicle to collect roughness data over a large area of the seafloor [13]. This data were collected along with bottom loss measurements conducted by both ARL:UT and the Acoustic Research Laboratory of the National University of Singapore (ARL-NUS) [14]. The second system was deployed by APL-UW and is mounted on a frame to measure high-resolution roughness over a smaller portion of the seafloor. This system also collected porosity data in the top 20 cm of the seafloor using a conductivity probe.

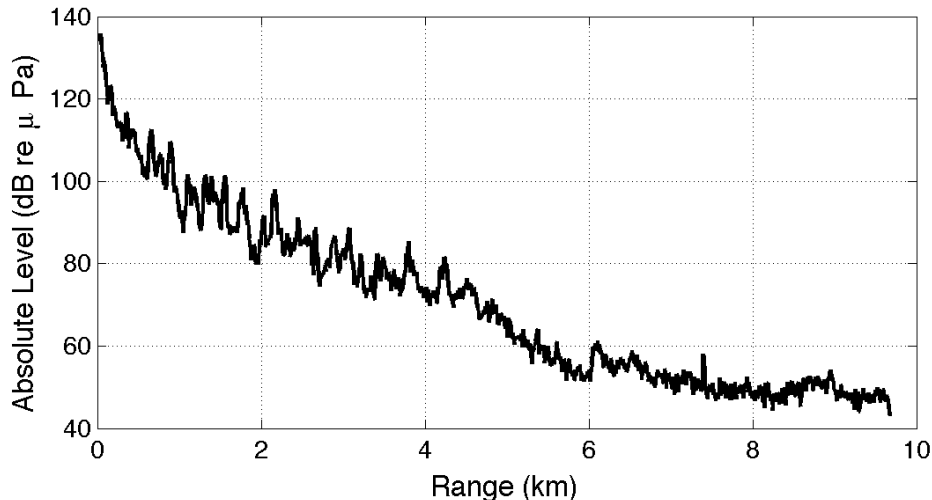


Fig. 2: Example of reverberation data measured at the TREX13 site during calm conditions (Provided by Jie Yang APL-UW).

In addition to the ARL:UT bottom loss measurements, reflectivity was also measured by ARL-Penn State and DRDC. Both of these measurements can indirectly provide sound speed in the sediment. Direct measurements of the sound speed were made using the APL-UW Sediment Acoustic Measurement System (SAMS) that measures the time-of-flight of signals transmitted from the seafloor to a receiver 3 m below the sediment interface.

Sub-bottom profiler data were collected by both the Institute for Geophysics at the University of Texas (UTIG) and DRDC. These data sets provide information about the sediment structure beyond 50 cm below the sediment interface. To characterize the upper portion of the sediment, the Naval Surface Warfare Center Panama City Division (NSWC-PCD) deployed the Buried Object Scanning Sonar (BOSS) along the main track [15]. This system is typically used to image mines and ordinance buried in the seafloor, but was deployed here to look for heterogeneities in the seafloor.

Finally, in an effort to characterize the fish activity at the experiment site, UW and the Wood's Hole Oceanographic Institute (WHOI) conducted several surveys of the site using an echo sounder to map the fish distribution as a function of time and location.

4. DATA ANALYSIS

Preliminary analysis of the acoustic data collected during this experiment has focused on understanding the role played by each term of equation (1) in reverberation under different conditions. To facilitate analysis, the reverberation data are being sorted and divided into the categories that emphasize a particular environmental impact: bottom reverberation under calm sea surface conditions (baseline dataset), reverberation under different wind conditions, reverberation dominated by biologics, and reverberation with both targets and clutter present. An example of the baseline reverberation data is shown in Fig. 2.

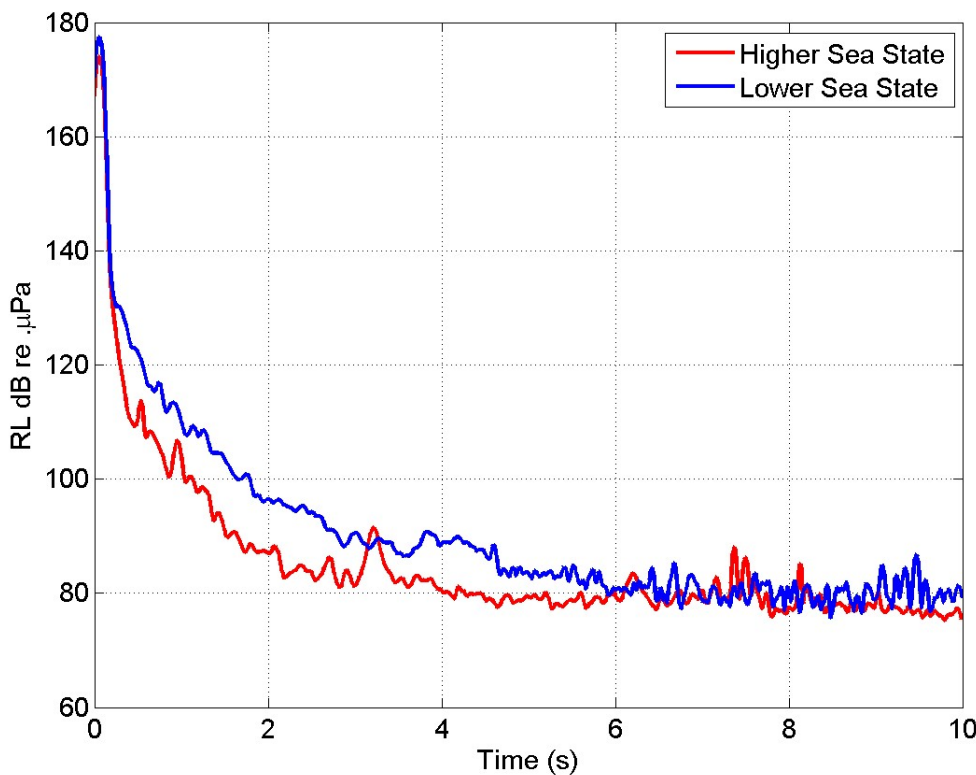


Fig. 3: Reverberation measured during TREX13 when there was a high sea state (red curve) and a low sea state (blue curve).

While the analysis is still in its early stages, some interesting results have already emerged. While the water depth changes only modestly along the main track, the reverberation level fluctuates on the order of 10 dB. These fluctuations are closely correlated to topographic changes, however the modest topographic variation is easily ruled out as the mechanism for the fluctuation. As seen in Fig. 1, the bottom has a ridge and swale topography with significant shell content on the southeast faces of the ridges and mud in the swales. The 400 kHz backscatter is strongest on these southeast faces while the 3 kHz backscatter is strongest in the mud-dominated swales. This strongly suggests that subbottom scattering at the mud locations is the cause of the reverberation fluctuations.

One of the main goals of the experiment was to collect reverberation under the influence of different sea surface conditions. While scattering from the seafloor dominates the backscatter in reverberation, models have shown that without taking into account both the coherent loss due to sea surface forward scatter and the incoherent scattered field, predictions of reverberation can be off by as much as 10 dB under a 15 knot wind [1]. Preliminary TREX13 data analysis from two different days, one calm, the other with high wind, show different reverberation levels qualitatively consistent with these predictions (Fig. 3). Systematic analysis of data under a wide range of wind and swell conditions will be performed to establish the importance of forward surface scattering.

REFERENCES

- [1] E.I. Thorsos, D. Tang, K.L. Williams, B.T. Hefner, and J. Yang, "Key Issues in Mid Frequency Reverberation Modeling and Experiments," In *Proceedings of the 4th conference on Underwater Acoustic Measurements*, 2011.
- [2] D. Francine and D.D. Ellis, "Data-model Comparisons of Reverberation at Three Shallow-water Sites," *IEEE JOE*, 22(2), pp. 309-316, 1997.
- [3] D.D. Ellis and J. R. Preston, "Comparison of model predictions with reverberation and clutter data in a range-dependent shallow water area," In 1st Underwater Acoustic Conference and Exhibition: Proceedings, J. S. Papadakis and L. Bjørnø, editors, pp. 465-472, 2013.
- [4] P. C. Hines and S. Murphy, "Continuous active and pulsed active sonar measurements in littoral waters," Underwater Acoustics Signal Processing Workshop (UASP), Alton Jones Campus, University of Rhode Island, 2013.
- [5] P. C. Hines, "Experimental comparison of continuous active and pulsed active sonars in littoral waters," In *1st Underwater Acoustic Conference and Exhibition: Proceedings*, J. S. Papadakis and L. Bjørnø, editors, 2013.
- [6] J. Choi, D. R. Dall'Osto, and P. H. Dahl, "Estimates of the bottom reflection coefficient involving vector sensor," *Presented at the 167th Meeting of the Acoustical Society of America*, 2014.
- [7] D. R. Dall'Osto and P. H. Dahl, "The influence of directional sea-surface waves on the acoustic intensity vector field," *Presented at the 167th Meeting of the Acoustical Society of America*, 2014.
- [8] D. R. Dall'Osto and P. H. Dahl, "Properties of the umov vector in shallow water and its dependence on sea surface conditions," *JASA*, 134(5), pp. 4111-4111, 2013.
- [9] J. Calantoni, K. Eldredge, T. Staple, A. Sheremet, and A. Penko, "Time series observations of seafloor roughness in the northern Gulf of Mexico 1: Sediment transport," *Presented at the Fall 2013 Meeting of the American Geophysical Union*, 2013.
- [10] T. Staples, U. Gravois, A. Sheremet, and J. Calantoni, "Time series observations of seafloor roughness in the northern Gulf of Mexico 2: Hydrodynamics". *Presented at the Fall 2013 Meeting of the American Geophysical Union*, 2013.
- [11] C. de Moustier and J. Calantoni, "Target detection with low-cost imaging sonars," In *Proceedings of the 2nd International Conference on Underwater Acoustics*, J. S. Papadakis and L. Bjørnø, editors, 2014.

- [12] C. de Moustier and B. J. Kraft, "High-frequency sediment acoustics over transitions from dense shell hash to mud: Repeat surveys at 7 frequencies from 150 khz to 450 khz," *JASA*, 134(5), pp. 4239–4239, 2013.
- [13] N. P. Chotiros, M. J. Isakson, J. N. Piper, and A. McNeese, "Sea floor roughness measured by a laser profiler on a ROV", In *Proceedings of OCEANS'14 MTS/IEEE TAIPEI*, 2014.
- [14] M. J. Isakson, N. P. Chotiros, J. N. Piper, and A. McNeese, "The effect of ocean bottom variability on transmission loss and reverberation," In *Proceedings of OCEANS'14 MTS/IEEE TAIPEI*, 2014.
- [15] S.G. Schock, and J. Wulf, "Buried object scanning sonar for AUVs," In *Proceedings of OCEANS 2003*, pp. 22-26, 2003.

Proceedings of the Institute of Acoustics

HIGH-FREQUENCY SCATTERING FROM A MUDDY SAND SEDIMENT WITH AN OVERLYING MUD LAYER.

Brian T. Hefner Applied Physics Laboratory, University of Washington, Seattle, WA, USA
Anatoliy Ivakin Applied Physics Laboratory, University of Washington, Seattle, WA, USA
Darrell R. Jackson Applied Physics Laboratory, University of Washington, Seattle, WA, USA

1 INTRODUCTION

While a significant amount of research has been conducted on the response of mines and munitions in sand sediments, the acoustic response of targets in muddy environments is not well understood. This lack of understanding exists despite the prevalence of this bottom type in very shallow water areas such as harbors and bays. This is largely due to the difficulty of collecting both acoustic measurements and sufficient environmental characterization to understand not only the acoustic response of the targets in the environment but the response of the sediment itself.

These challenges motivated the selection of the Bay Experiment (BayEx14) site which took place in St. Andrew's Bay in the spring of 2014 and was jointly sponsored by the US Office of Naval Research (ONR) and the Strategic Environmental Research and Development Program (SERDP). The experiment site was in 7 m of water and the seafloor consisted of a 10–15 cm thick mud layer on top of a sand/mud bottom. This sand/mud basement was rigid enough to support the placement of mechanical and electronic systems on the bottom and prevent the acoustic targets from sinking into the mud. This made it possible to deploy the suite of instruments that had been developed for previous experiments in areas with sand bottoms, such as the Sediment Acoustics Experiments in 1999 (SAX99)¹ and 2004 (SAX04)² and the more recent Target and Reverberation Experiment in 2013 (TREX13).³

The primary thrust of BayEx14 was to use synthetic aperture sonar to study target scattering in a sand/mud environment. In addition to these measurements, a second set of data was collected to look at mid and high-frequency backscattering from the seafloor in the absence of the targets. The goal of this work was to understand the dominant scattering mechanisms in this environment, how the introduction of the mud layer affects the scattering response, and to support the development of an acoustic seabed classification technique. To interpret the data and develop scattering models for this sediment, extensive environmental characterization was performed at this site as well. This paper presents the inversion and analysis of multibeam sonar data using the environmental characterization collected at the site.

2 MEASUREMENTS

2.1 MULTIBEAM SONAR

The experiment took place in the southeast arm of St. Andrew's Bay near Panama City Beach, Florida (Figure 1). A majority of the data was collected from May 8 to May 27 while the R/V Sharp was in a four-point moor at the experiment site. Instruments and acoustic systems deployed on the bottom were cabled to the ship which also acted as a platform for the deployment of divers to assist in the setup and operation of the equipment. Despite efforts by the divers to minimize contact with the seafloor, dive operations significantly disturbed the seafloor, artificially modifying the environment. In

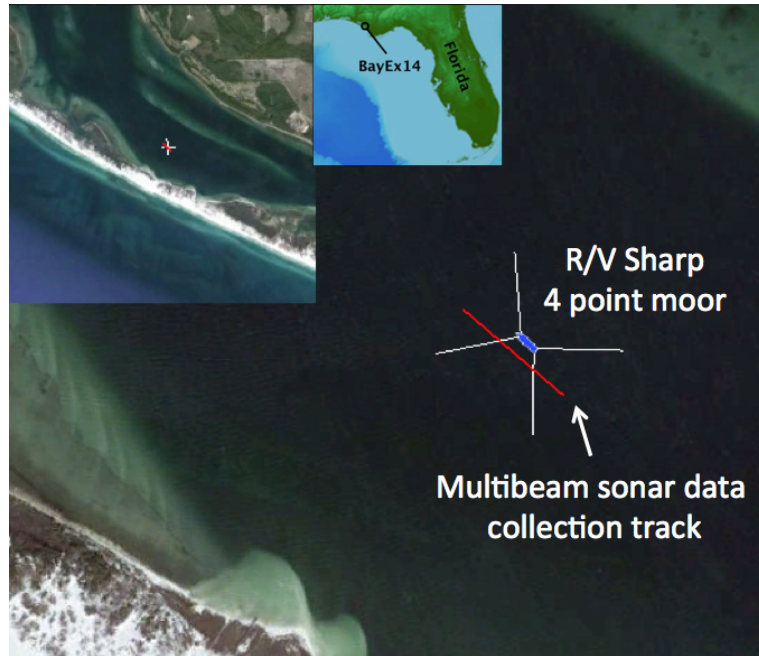


Figure 1: Location of the Moored R/V Sharp and the multibeam sonar data collection track.

anticipation of this disturbance, the multibeam sonar collected backscatter data prior to the arrival of the R/V Sharp at the experiment site.

The multibeam sonar used was a Teledyne-RESON 7125 which is usually operated at either 200 kHz or 400 kHz depending on the depth of the seafloor. The beam width at 200 kHz is 2 degrees along track and 1 degree across track. The beam width at 400 kHz is 1 degree along track and 0.5 degrees across track. The beams extend across a full swath-width of 140 degrees. For this work, the software used to run the 7125 was modified to operate at 20-25 kHz increments from 180 kHz to 420 kHz. The beam widths at each frequency varied between the two extremes at 200 and 400 kHz.

In typical bathymetric measurements using a multibeam sonar, only the timing and magnitude of the peak scattered signal is recorded for each beam. In this project, which seeks to develop a seabed classification technique, the full time series data was collected for each beam. To collect this time series data at the 11 frequencies of interest, a single 200 m long track was chosen to be the focus of the data collection. This track ran parallel to the subsequent orientation of the ship and passed to its southeast as indicated in Figure 1.

The data collected by the multibeam was then processed using an inversion technique developed over the course of several experiments including TREX13.⁴ The ultimate goal of any seabed classification technique is to determine the intrinsic physical properties of the sediment such as density, sound speed, and porosity. As opposed to the empirical approaches used in other classification techniques, in the inversion used here the acoustic data collected with the multibeam was used to first obtain estimates of the interface scattering strength, volume scattering, and attenuation. These parameters are estimated by fitting a model for the echo intensity time series, as in.⁵⁻⁸ This approach separates the interface and volume scattering, which is possible due to the high directivity of the multibeam sonar. The estimates of the interface scattering strength can then be used to estimate the roughness parameters and the impedance of the sediment. Further estimates of the sediment parameters such as porosity and density can be obtained by using these parameters with published empirical relationships.

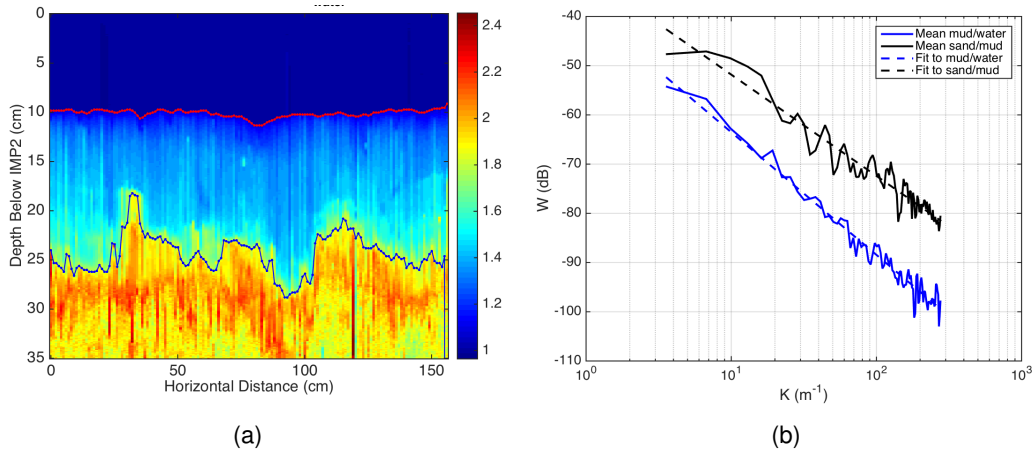


Figure 2: (a) Formation factor measured by the IMP2 conductivity probe in St. Andrew's Bay. The red and black lines indicate the mud/water interface and the sand/mud interface respectively. (b) The roughness power spectra corresponding to the surfaces indicated in (a).

2.2 ENVIRONMENTAL CHARACTERIZATION

While the R/V Sharp was in a four-point moor, diver cores and conductivity data were collected in order to determine the sediment properties. This data was collected on the south side of the ship to coincide with the center of the MBES track. Two sets of diver cores were collected; one capturing only the mud layer and the other capturing only the sand/mud basement. Both sets were analyzed for porosity and density. For the mud layer, the density was $\rho_m = 1.26 \pm 0.06 \text{ g/cm}^3$ and the porosity was $\beta_m = 81\% \pm 1\%$. The underlying sand had a density of $\rho_s = 2.10 \pm 0.02 \text{ g/cm}^3$ and a porosity of $\beta_s = 40\% \pm 1\%$.

The conductivity data was collected using the In-situ Measurement of Porosity (IMP2) system.⁹ This system uses a single constant-current electrode that is scanned through the sediment in a 2D plane using a horizontal and vertical positioning system mounted on a frame that rests on the seafloor. The probe can be inserted 25 cm into the sediment in 1 mm increments and at 1 cm horizontal steps up to 4 m. At each position the output voltage of the probe is recorded which is inversely proportional to the mean conductivity over the resolution cell of the electrode. The “formation factor,” F , is typically found by taking the ratio of the voltage measured in the sediment to the voltage measured in the overlying water. From the formation factor, the sediment porosity is calculated according to an empirical relation known as Archie's Law,

$$\beta = \frac{1}{F^{1/m}} \quad (1)$$

where m is a constant for a given sediment. This constant is determined by calibrating the probe using a sediment sample that is later dried and weighed to determine the bulk porosity. The spatial distribution of the porosity fluctuations can then be calculated and, if the sediment material properties are known, the density fluctuations can also be calculated. These are used to determine the fluctuation power spectrum, which is used as an input to perturbation theory for volume scattering from the sediment.

An example of the formation factor measured at the BayEx14 site is shown in Figure 2(a). The mud layer (light blue) is clearly resolved by the conductivity probe and has a thickness of $H_{mud} = 13.4 \pm 1.6$ cm, determined from this and other probe measurements at the site. The conductivity probe data also indicates the locations of the mud/water and sand/mud boundaries, from which the 1D roughness power spectra can be calculated as shown in Figure 2(b). The sand/mud boundary is significantly rougher than the mud/water boundary by 10–20 dB in spectral level and roughly 5 dB higher than the roughness measured for typical sand sediments. It's not clear what mechanism produces the

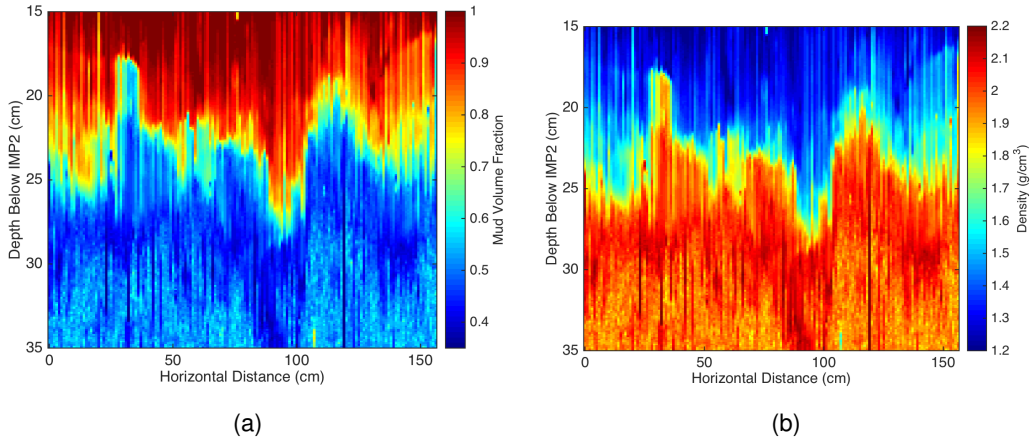


Figure 3: (a) Mud volume fraction across the sand/mud interface. (b) The sediment density across the sand/mud interface.

roughness at this boundary, but it is likely that the mud preserves the roughness from feeding fish, slumping, and hydrodynamic actions.

The boundary between the mud and sand is also not as sharp as the mud/water boundary. This indicates that the sediment is actually a mix of mud and sand, the ratio of which changes as the boundary is crossed, and suggests an alternative approach to interpreting the formation factor. The particle size in the solid component of the mud is much smaller than the size of the sand grains, $a_{mud} \ll a_{sand}$. It seems reasonable, given the nature of the sediment, to assume that the mud permeates the pores between the sand grains. If the density of the mud is

$$\rho_m = \beta_m \rho_f + (1 - \beta_m) \rho_{mg}, \quad (2)$$

where β is the porosity of the mud, ρ_f is the density of the fluid, and ρ_{mg} is the density of the solid component of the mud, then the density of the sediment can be written as

$$\rho = \Phi \rho_m + (1 - \Phi) \rho_{sg}, \quad (3)$$

where Φ is the volume fraction of the mud and ρ_{sg} is the density of the sand grains. Using (2) and (3), the actual porosity or volume fraction of water at any point in the sediment is $\beta = \Phi \beta_m$.

To analyze the conductivity probe data, recall that the voltage, V , measured by the probe is inversely proportional to the mean conductivity σ over the resolution cell of the electrode,

$$V = \frac{I}{4\pi\sigma a}, \quad (4)$$

where I is the system current and a is the radius of the probe. Assuming that the conductivity of the mud does not change within the pores of the sediment, we can define a new formation factor as

$$F = \frac{\sigma_m}{\sigma(\mathbf{r})} = \frac{V(\mathbf{r})}{V_m}, \quad (5)$$

where σ_m and $\sigma(\mathbf{r})$ are the conductivities in mud and at position \mathbf{r} and where V_m and $V(\mathbf{r})$ are the voltages in mud and at position \mathbf{r} . With this definition of the formation factor, we can now use Archie's law to determine the mud volume fraction,

$$\Phi = \frac{1}{F^{1/m}}. \quad (6)$$

This assumes that the Archie's law relationship is valid across the full range of mud volume fractions (0.4– 1.0).

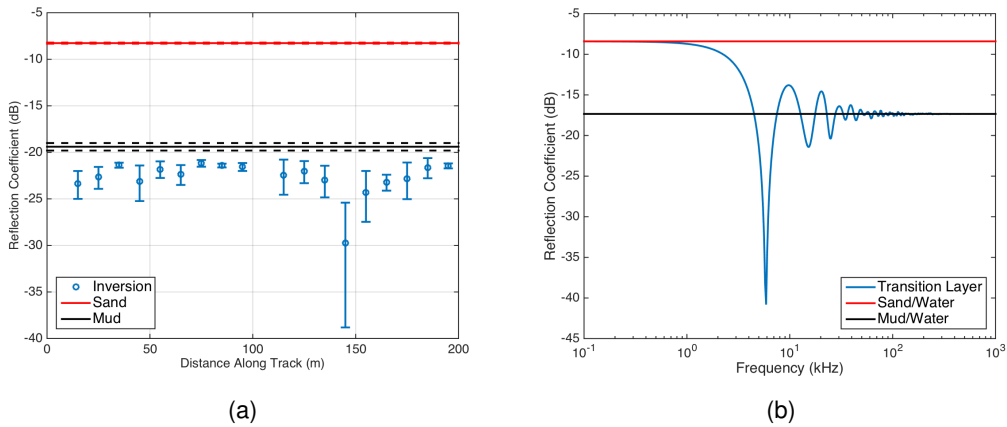


Figure 4: (a) Normal incidence reflection measured from the sand/mud interface compared to the expected reflection coefficients for a mud/water and a sand/mud interface. (b) Model result for normal incidence reflection from the density profile shown in Fig. 5.

To apply this to BayEx14 conductivity probe data, the formation factor is recalculated by taking the voltage values at 15 cm, where the mud voltages are fairly stable, and divide all of the voltages by these values. Using the porosity values measured using the diver cores in mud and the sand, the mean mud volume fraction in the sand is $\Phi = \beta_s/\beta_m = 0.49$. Using this value and the mean of all formation factor values that are deeper than 30 cm, $m = 0.49$ can be found from Archie's law. The mud volume fraction can now be calculated across the boundary (Figure 3(a)) and from this, using (3), the sediment density can also be found (Figure 3(b)).

The assumption that the mud permeates the pores in the sand layer is consistent with observations made by divers at the site and with visual inspections of the diver cores however it remains to be confirmed by a quantitative analysis of diver cores from the site.

3 DATA/MODEL COMPARISONS

As discussed in Section 2.1, a number of sediment properties are determined by the MBES algorithm. In this paper, we will focus on two of the inversion outputs: the reflection coefficient and the volume scattering cross section.

3.1 NORMAL REFLECTION

The inversion algorithm makes a number of simplifying assumptions about the structure of the sediment in order to limit the number of parameters over which one must search. One of these assumptions, which the BayEx14 sediment violates, is that the sediment can be treated as a half-space. As a result, while the signal reflected from the sediment shows a weak initial return from the mud and a second, stronger return from the sand, the algorithm chooses the larger of the two and assumes that it is the return from the half-space. Since it uses the signal scattered from the sand/mud interface, it is reasonable to expect that the reflection coefficient determined from that signal should correspond to that interface. As can be seen in Figure 4(a), the opposite occurs: the reflection coefficient more closely matches that of the mud/water interface.

To understand why this might be the case, it is necessary to take into account the transition layer at the sand/mud boundary.¹⁰ To determine how the density and sound speed vary across this boundary, the roughness of this boundary is first removed by realigning the vertical profiles such that the interface is flattened as in Figure 5. Once this has been done, the mean density and, through a similar procedure,

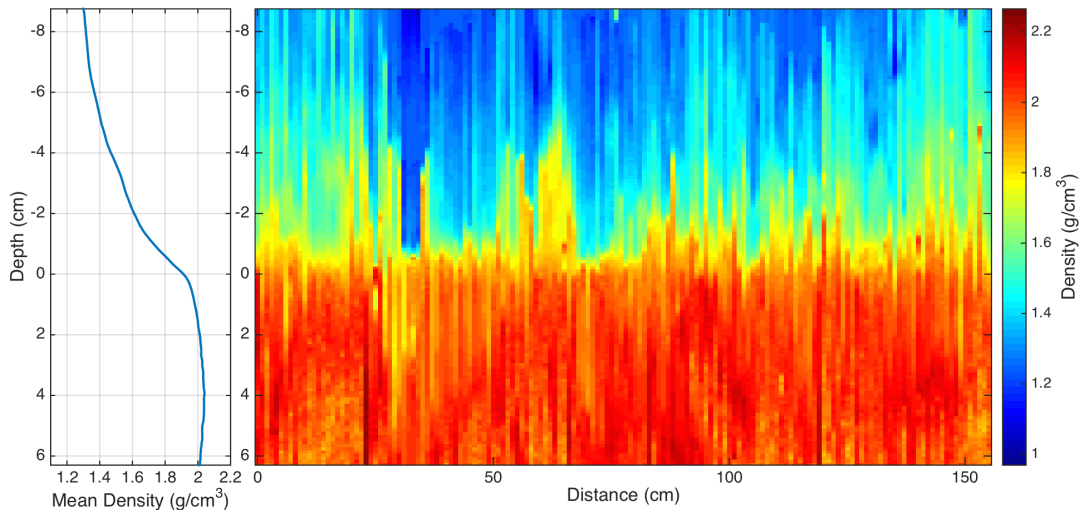


Figure 5: Sediment Density after each vertical density profile has been shifted such to remove the roughness at the sand/mud interface. The left plot shows the mean density across this realigned interface.

the mean sound speed as a function of depth can be found. This profile can be approximated as a sequence of very thin layers for which the reflection coefficient can be determined.¹¹ The results of this calculation are shown as a function of frequency in Figure 4(b).

At low frequencies, the reflection coefficient corresponds to that of a sand/water interface. As the frequency increases and the wavelength approaches the thickness of the layer, the reflection coefficient decreases and reaches a strong minimum value when the thickness is approximately a quarter wavelength. Beyond this, the reflection coefficient approaches the mud/water value at high frequencies. This occurs since the density is changing at scales much larger than a wavelength and as a result the wave passes smoothly through the boundary. The only reflection therefore occurs at the top of the layer. The reflection values are actually slightly lower than the mud/water value and this is likely due to the small transition layer at the mud/water interface that can be seen in Figure 2(a) but is not accounted for in the model. Also, in using the profile in Fig. 5, the model assumes a constant thickness for the mud layer. As indicated in Fig. 2(a), the thickness of the layer varies with location and this will have the effect of smoothing the low to high frequency transition, removing the the strong nulls in the reflection coefficient.

3.2 VOLUME SCATTERING

The volume scattering strength determined by the inversion algorithm is shown in Figure 6(b). The algorithm again treats the sediment as a half-space and assumes that the volume scattering cross section is constant throughout the half space. Shown in the figure are two different results; the first assumes that the sand/mud boundary is abrupt while the second assumes that it has the profile shown in Figure 5. This slightly lowers the volume scattering strength (~ 1 dB).

To model the scattering strength, the density data shown in Figure 2(b) is used to determine the density fluctuations in the sand sediment sediment. Using several IMP2 data sets from different locations, the resulting 1D power spectra are shown in Figure 6(a). These are converted to 3D spectra and used in the small perturbation scattering approximation.¹² The model results are compared to the inversion in Figure 6 where they underpredict the inversion results by 5–10 dB.

One possibility for this discrepancy is that since the interface is very rough and sitting in the transition layer, it becomes difficult to discriminate between interface scattering and volume scattering along

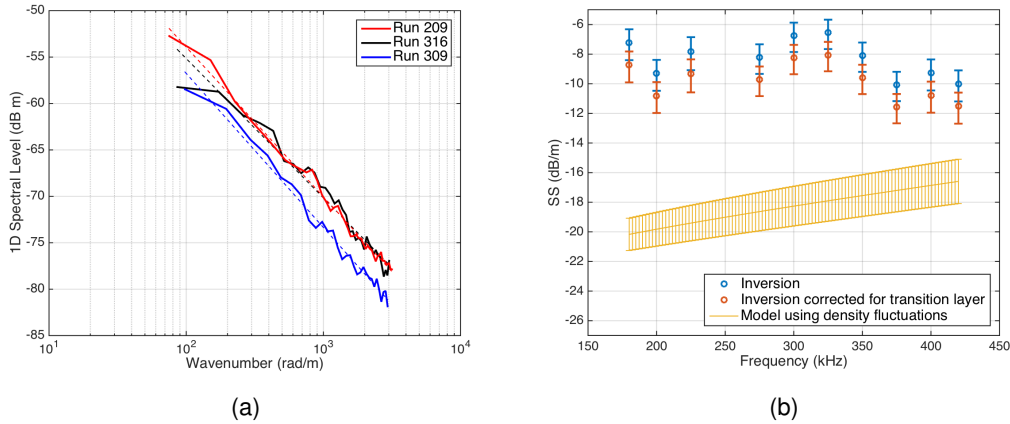


Figure 6: (a) Heterogeneity spectrum measured in the sand layer. (b) The volume scattering strengths determined from the inversion compared to the small perturbation approximation predictions.

this interface since the boundary is no longer clear. The inversion may be treating this interface as volume scattering where the scattering based on the density fluctuations is not taking this into account. This hypothesis is also consistent with spectral inversions of the roughness scattering strength where the inversion slightly under estimates the sand/mud interface roughness spectrum. This is also supported by inversions that were performed using a more complex model. This model estimates volume scattering strengths for two regions, a 15 cm layer starting at the sand/mud interface and the half space below. This half space contains the regions in which the heterogeneity was measured. For the more complicated inversions, volume scattering strengths for the 15 cm layer are similar to those obtained from the simpler inversion, but those for the lower half-space agree with ground-truth within measurement uncertainties. Thus, the inversion agrees with ground truth when it isolates the region in which the ground-truth measurements were made.

4 CONCLUSIONS

The BayEx14 site, like many sediments, has a deceptively simple description: a 13 cm mud layer over a sand bottom. Using a conductivity probe which could measure the density profile in 2D planes through the mud layer and into the sand, this “simple” sediment was found to have a level of complexity that, if not accounted for, would lead to erroneous conclusions about the nature of the acoustic interactions. This was seen in both the data/model comparisons for the normal incidence reflection coefficient and for the scattering strengths. In the first case, the reflection model needed to account for the transition layer at the sand/mud boundary and, for the volume scattering, the inversion needed to be modified to take into account the ambiguous nature of the scattering at the transition layer. An alternative may be to use a unified approach to modeling the scattering at the boundary such as that developed in Ref. 13.

5 ACKNOWLEDGEMENTS

This work was supported by the Strategic Environmental Research and Development Program and the US Office of Naval Research. The authors would also like to thank Dr. Gorm Wendelboe and Teledyne-RESON for providing the multibeam sonar and the technical assistance necessary for its deployment.

Proceedings of the Institute of Acoustics

6 REFERENCES

1. E. I. Thorsos, K. L. Williams, N. P. Chotiros, J. Christoff, K. Commander, C. Greenlaw, D. Holliday, D. R. Jackson, J. Lopes, D. McGehee, J. Piper, M. Richardson, and D. Tang. An overview of SAX99: acoustic measurements. *IEEE J. of Ocean. Eng.*, 26(1): pp. 4–25, (2001).
2. K. L. Williams, D. R. Jackson, D. Tang, K. B. Briggs, and E. I. Thorsos. Acoustic Backscattering From a Sand and a Sand/Mud Environment: Experiments and Data/Model Comparisons. *IEEE J. of Ocean. Eng.*, 34(4): pp. 388–398, (2009).
3. B. T. Hefner and D. Tang. Overview of the reverberation component of TREX13. In *Proceedings of the 2nd International Conference and Exhibition on Underwater Acoustics*, 22-27 June, Rhodes, Greece, (2014).
4. D. R. Jackson, B. T. Hefner, A. N. Ivakin, and G. Wendelboe. Seafloor characterisation using physics-based inversion of multibeam sonar data. In *Proceeding of the 11th European Conference on Underwater Acoustics*, pp. 1571–1576, (2012).
5. E. Pouliquen and X. Lurton. Seabed identification using echo-sounder signals. *ECUA 1992*, : pp. 535–538, (1992).
6. D. D. Sternlicht and C. P. de Moustier. Time-dependent seafloor acoustic backscatter (10-100 kHz). *J. Acoust. Soc. Am.*, 114: pp. 2709–2725, (2003).
7. D. D. Sternlicht and C. P. de Moustier. Remote sensing of sediment characteristics by optimized echo-envelope matching. *J. Acoust. Soc. Am.*, 114: pp. 2727–2743, (2003).
8. C. De and B. Chakraborty. Acoustic characterization of seafloor sediment employing a hybrid method of neural network architecture and fuzzy algorithm. *Geoscience and Remote Sensing Letters, IEEE*, 6(4): pp. 743–747, (2009).
9. D. Tang. Fine-scale measurements of sediment roughness and subbottom variability. *IEEE J. of Ocean. Eng.*, 29: pp. 929–939, (2005).
10. A. Lyons and T. H. Orsi. The effect of a layer of varying density on high-frequency reflection, forward loss, and backscatter. *IEEE J. of Ocean. Eng.*, 23(4): pp. 411–422, October (1998).
11. L. M. Brekhovskikh and I. U. P. Lysanov. *Fundamentals of Ocean Acoustics*. Modern Acoustics and Signal Processing. Springer, (2003).
12. D. R. Jackson and M. Richardson. *High-Frequency Seafloor Acoustics*. Springer, New York, NY, (2006).
13. A. Ivakin. Unified approach to volume and roughness scattering. *J. Acoust. Soc. Am.*, 103(2): pp. 827–837, (1998).

REPORT DOCUMENTATION PAGE

Form Approved
OMB No. 0704-0188

The public reporting burden for this collection of information is estimated to average 1 hour per response, including the time for reviewing instructions, searching existing data sources, gathering and maintaining the data needed, and completing and reviewing the collection of information. Send comments regarding this burden estimate or any other aspect of this collection of information, including suggestions for reducing the burden, to Department of Defense, Washington Headquarters Services, Directorate for Information Operations and Reports (0704-0188), 1215 Jefferson Davis Highway, Suite 1204, Arlington, VA 22202-4302. Respondents should be aware that notwithstanding any other provision of law, no person shall be subject to any penalty for failing to comply with a collection of information if it does not display a currently valid OMB control number.
PLEASE DO NOT RETURN YOUR FORM TO THE ABOVE ADDRESS.

1. REPORT DATE (DD-MM-YYYY)			2. REPORT TYPE		3. DATES COVERED (From - To)	
4. TITLE AND SUBTITLE			5a. CONTRACT NUMBER			
			5b. GRANT NUMBER			
			5c. PROGRAM ELEMENT NUMBER			
6. AUTHOR(S)			5d. PROJECT NUMBER			
			5e. TASK NUMBER			
			5f. WORK UNIT NUMBER			
7. PERFORMING ORGANIZATION NAME(S) AND ADDRESS(ES)					8. PERFORMING ORGANIZATION REPORT NUMBER	
9. SPONSORING/MONITORING AGENCY NAME(S) AND ADDRESS(ES)					10. SPONSOR/MONITOR'S ACRONYM(S)	
					11. SPONSOR/MONITOR'S REPORT NUMBER(S)	
12. DISTRIBUTION/AVAILABILITY STATEMENT						
13. SUPPLEMENTARY NOTES						
14. ABSTRACT						
15. SUBJECT TERMS						
16. SECURITY CLASSIFICATION OF:			17. LIMITATION OF ABSTRACT	18. NUMBER OF PAGES	19a. NAME OF RESPONSIBLE PERSON	
a. REPORT	b. ABSTRACT	c. THIS PAGE			19b. TELEPHONE NUMBER (Include area code)	